Composites Part B 172 (2019) 564–592

Contents lists available at ScienceDirect

Composites Part B

journal homepage: www.elsevier.com/locate/compositesb

Effect of patterned inclusions on the fracture behavior of ceramic composites

Congjie Wei [a], Chenglin Wu [a,*], Charles Wojnar [b]

[a] Department of Civil, Architectural, and Environmental Engineering, Missouri University of Science and Technology, Rolla, MO, USA
[b] Computational Engineering Division, Lawrence Livermore National Laboratory, Livermore, CA, USA

ARTICLE INFO

Keywords:
Ceramic-matrix composites
Particle-reinforcement
Phase-field implementation
Mixed-mode fracture

ABSTRACT

Developments in additive manufacturing have enabled the reinforcement of ceramic composites across the scales. Understanding the fracture behavior of such composites is critical for structural design and engineering. However, systematic investigations on the relationship between the patterning characteristics and the effective fracture properties have been scarce. This work proposes a mixed-mode phase field model to investigate the effects of elastic modulus and pattern characteristics of circular inclusions on the fracture behavior of a ceramic composite beam. The modeling results have shown that the stiff and compliant inclusions can either repel or attract the crack. The extent of repelling and attraction can be controlled by altering the pattern characteristics. In addition, utilizing the relationship between the pattern characteristics and resulting fracture path, fracture growth can be controlled with appropriate inclusion properties. The targeted enhancement in fracture toughness can also be predicted using an effective fracture model linked with the underlying fracture path computed by the proposed mixed-mode phase field model.

1. Introduction

Describing brittle fracture in ceramics has developed from the initial notion of fracture toughness introduced by Griffith [1] to the notion of effective toughness in ceramic composites in recent decades [2–7]. Ceramic composites provide a means to increase the overall toughness of a structure beyond a homogeneous material due to the presence of toughening mechanisms such as crack deflection, branching, and repelling [8]. With continually advancing manufacturing methods, a multitude of complex composite arrangements can be created and geared towards increasing toughness. To discover optimal composite arrangements, the analysis and simulation of how cracks propagate through heterogeneous media is required.

Closed form analytical solutions for the effective fracture toughness of laminated composites was carried out by Gao [6,9,10]. The approach provided an efficient way to observe how composite geometries and properties changed the effective response but was of course limited by the assumptions made including the simplified geometry and small elastic mismatch. In addition, this approach mainly dealt with cracks interacting with finite strips or layered composites. Bower and Ortiz (1991) extended Gao's theory and applied the finite perturbation method to analyze the enhancing effect of adding small quantities of tough particles within a solid material in three-dimensions [2]. The effect of these tough particles on fracture growth was mainly reflected in the crack bridging mechanisms. However, the stress intensity factor based linear elastic fracture mechanics (LEFM) approach has challenges in analyzing complex heterogeneous patterns, which can now be produced with advanced manufacturing methods. Yu et al. (2009) presented the derivation of an interaction (energy) integral to compute mixed-mode stress intensity factors in heterogeneous materials by obtaining the equivalent domain integral [11]. This approach has advantages over the perturbation analysis (small elastic mismatch) as the required computational time can be significantly reduced and could be applied to systems with larger elastic mismatch. However, this method still cannot analyze complex geometry, hence, numerical fracture models have also gained more widespread use in studying the fracture behavior of composites because they can be applied cases with complex heterogeneities.

The most-widely accepted numerical methods for fracture modeling of composite materials are the discontinuous Galerkin (DG) method, the cohesive zone model (CZM), and the smeared cracking model (SCM)) [12–18]. The SCM, especially its latest advancement, the phase-field

* Corresponding author.
E-mail address: wuch@mst.edu (C. Wu).

https://doi.org/10.1016/j.compositesb.2019.05.058
Received 23 January 2019; Received in revised form 2 May 2019; Accepted 5 May 2019
Available online 14 May 2019
1359-8368/

model, has shown promise recently for addressing limitations of the other numerical methods. Its main advantages over DG and CZM include: (1) there is no requirement of an initial crack (which may not be known a-priori), (2) it has the capability to modeling fracture branching and coalescing, and (3) it has relatively low requirements on mesh configurations (such as element type, nodes number and interpolation order).

The concept of regularizing fracture (in SCM) into a continuous field, representing the state of material, started firstly from Rashid's work of introducing stress release to the constitutive model [19]. Instead of creating a discontinuity for the crack, the constitutive relationship can be altered, or softened, based on the additional continuous field. After decades of development, this method has been applied increasingly within the field of materials science and fracture mechanics. Francfort and Marigo [20] adopted the concept of minimization of potential energy, consisting of internal strain energy and surface energy, regarding displacement and crack topology. The extra scalar field representing the damage related material state was introduced by Bourdin [21]. In recent years, this method has been widely employed for several aspects of fracture related themes including brittle dynamic fracture and thermo-mechanical fracture using numerical and analytical approaches [16,22–24]. Hossain et al. (2014) studied the effective toughness of heterogeneous media with concept of macro homogenization via surfing boundary conditions [7]. However, the applied phase field approach only considered mode-I fracture, which could oversimplify the fracture mechanism [25,26]. Nevertheless, it was concluded that the computational approach with homogenization shows higher efficiency in terms of memory usage compared with fully mapping [27] when investigating the fracture behavior of composite materials with patterned heterogeneity.

Generally, phase field models for fracture utilize a scalar damage variable. The damage variable used here is $\phi \in [0, 1]$, where $\phi = 0$ corresponds to a virgin (undamaged) state and $\phi = 1$ corresponds to a completely fractured state. This approach introduces damage in a continuous manner removing the challenges associated with discontinuities introduced by the fracture propagation. With the damage variable introduced, it is necessary to relate it to the mechanics of the structure. One common approach is to define the damage variable evolution from an energy perspective [16,28] with following process. First the relation between the damage variable and the stored strain energy density must be defined. Then, one adds to the total stored energy the energy required to create the new surface. Binomial and monotonic functions are among the most widely adopted functional forms for strain energy degradation due to fracture [29].

However, a common assumption when choosing the strain energy density degradation function is to assume fractures propagate solely in mode I. While this approach gives reasonable results for homogenous materials, the effect of complex stress fields in heterogeneous materials (in ceramics in particular) are not captured [30,31]. There have been a limited number of studies including mixed-mode fracture phase-field models, such as for anisotropic rocks [26,30] and cementitious materials [25]. However, the formulations in these works were not derived based on the commonly adopted power-law criterion for ceramic materials, which are in close agreement with the available experimental

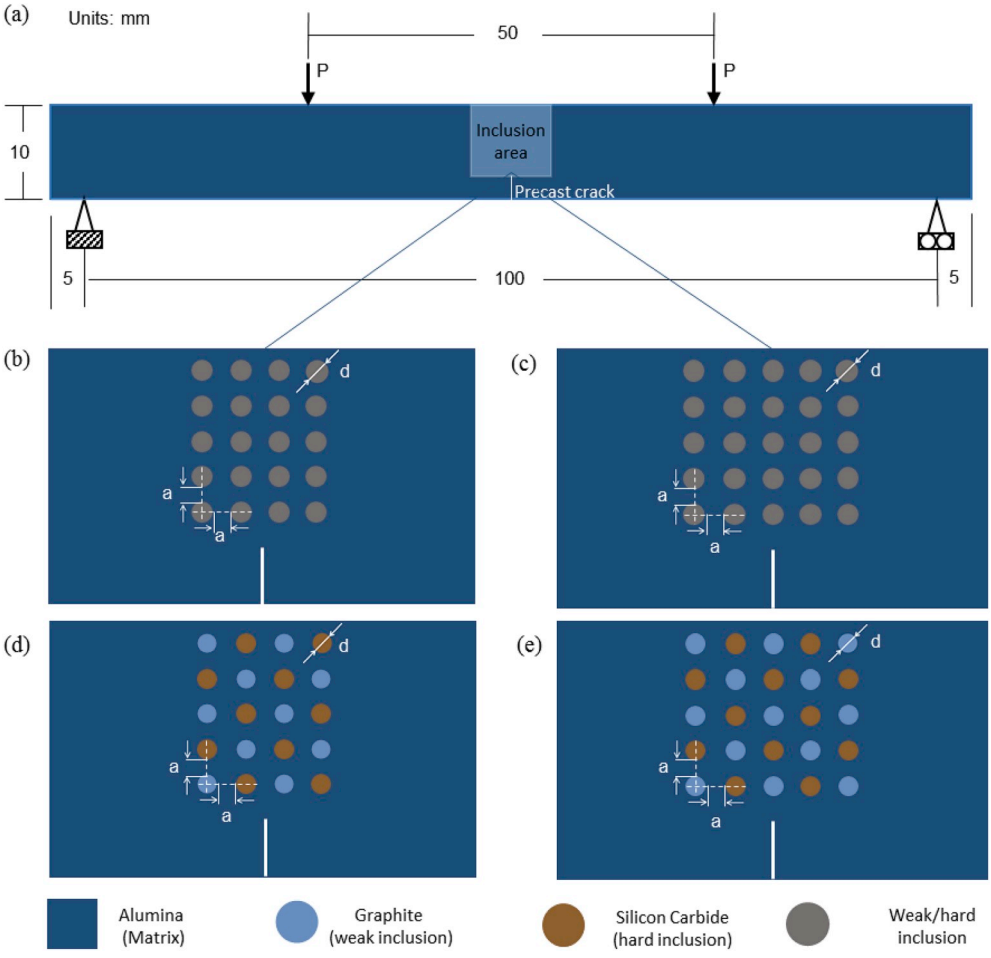

Fig. 1. Composite beam in 4-point bending configuration. The specimen geometry and boundary conditions are shown in (a). Inclusion arrangement for series c2 and s1 is shown in (b). Inclusion arrangement for series c1 and s2 is shown in (c). Inclusion arrangement for series h1 is shown in (d). Inclusion arrangement for series h2 and h3 is shown in (e). The inclusion spacing is denoted by a and the inclusion diameter is denoted by d.

results [5,32,33]. This leads to less accurate fracture growth predictions.

To obtain a more accurate picture of how cracks propagate in two-phase composites with varying designs, a mixed-mode phase field model was developed, implemented in ABAQUS, and then validated (discussed in Appendix A2). Using this model, crack propagation through a series of composite specimens with different inclusion geometries and properties were simulated to gain insight into how to optimize the composites for increased overall toughness. Secondary development of user element and user material subroutines, UEL and UMAT, respectively, within the commercial software ABAQUS was adopted for the numerical implementation. The fracture resistance was characterized for all cases using effective fracture variables defined from a volumetric homogenization scheme and domain integral. The results show a significant enhancement in fracture toughness with both compliant and stiff patterned inclusions. In addition, a guided fracture growth was observed with combined compliant and stiff inclusion patterns, revealing a means to tailor and optimize the toughness of composites.

2. Phase-field modeling for mixed-mode fracture

The main concept of the phase-field method is to convert discontinuities in field variables due to the presence of cracks to continuous fields by regularizing the crack into a continuous field. The scalar phase-field variable is introduced as, ϕ, ranging from 0 to 1, where 0 means the material point has not been damaged and 1 means the material is fully damaged. The total internal energy is (considering the phase-field induced damage in strain energy) as (cf. Eq. (A.2))

$$U(\phi,u)=\int_{\Omega}\left[(1-\phi)^2+k\right]\psi(\varepsilon)d\Omega+\int_{\Omega}\frac{G_c}{2}\left[\ell_0\phi_{,i}\phi_{,i}+\frac{1}{\ell_0}\phi^2\right]d\Omega \tag{1}$$

where $\psi(\varepsilon)$ is the elastic strain energy density (of the undamaged material), ε is the small strain tensor, G_c is the critical energy release rate, ℓ_0 is the regularization scale parameter (controls the crack thickness), and k is a parameter to keep the system well-conditioned during the simulation. Note that index notation and summation convention are implied, and commas denote derivatives with respect to the spatial coordinates. The first term on the right-hand side denotes the reduced elastic strain energy due to an increase in ϕ. The second term on the right-hand side represents the regularized surface energy related to fracture growth. The potential energy is then given by the difference between the stored internal energy and work done by external forces,

$$\Pi=U-V, \tag{2a}$$

where the work done by an external body force, b_i, and surface traction, t_i, is given by

$$V=\int\Omega\rho b_i u_i d\Omega+\int\partial\Omega_t t_i u_i d\partial\Omega, \tag{2b}$$

with ρ denoting the density. Applying the Principle of Minimum Potential Energy, the equilibrium solutions for the displacement field and phase-field damage parameter are those that minimize the potential energy. The potential energy can be minimized by taking its first variation with respect to displacement and phase-field parameter (see Appendix A1) to obtain the following governing differential equations (or Euler-Lagrange equations) as given in Eq. A.14a-e

$$\sigma_{ij,j}+b_i=0 \text{ in } \Omega \tag{3a}$$

$$\sigma_{ij}n_j=t_i \text{ on } \partial\Omega_t \tag{3b}$$

$$u_i=\bar{u}_i \text{ on } \partial\Omega_u \tag{3c}$$

$$2(\phi-1)\sqrt{\left(\frac{\psi_{\mathrm{I}}(x,\varepsilon)}{G_{\mathrm{I}c}}\right)^2+\left(\frac{\psi_{\mathrm{II}}(x,\varepsilon)}{G_{\mathrm{II}c}}\right)^2}+\frac{\phi}{\ell_0}=\ell_0\phi_{,ii} \text{ in } \Omega \tag{3d}$$

$$\phi_{,i}\,n_i=0 \text{ on } \partial\Omega, \tag{3e}$$

where $\sigma_{ij}=\frac{\partial\varphi}{\partial\varepsilon_{ij}}$ is the Cauchy stress tensor and G_{Ic} and G_{IIc} are the critical energy release rate in mode I and II, respectively. Also, the applied

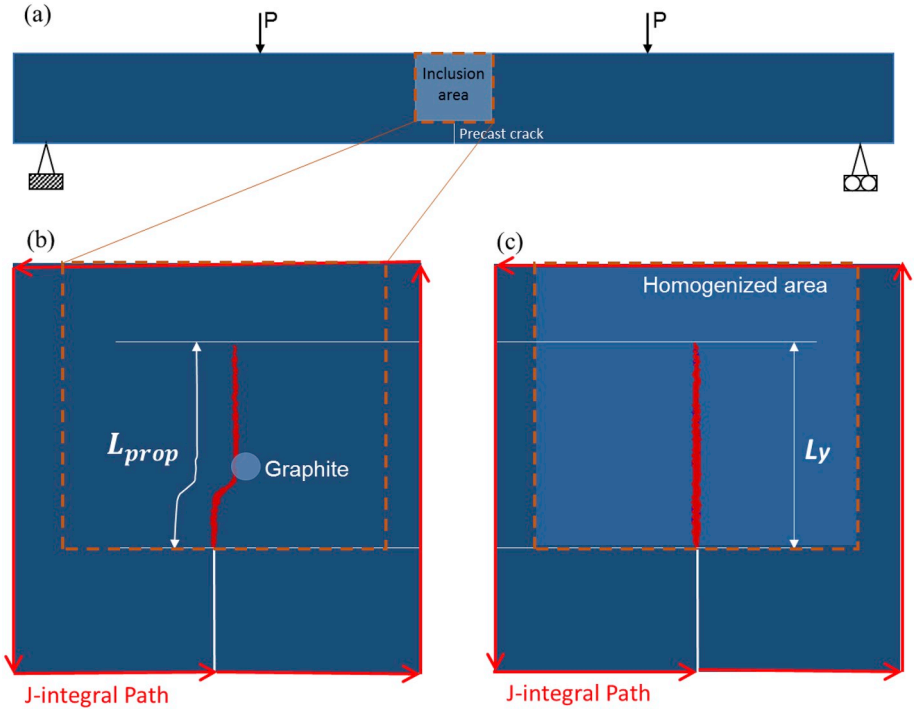

Fig. 2. Graphical illustration of the material homogenization scheme and calculation of effective fracture toughness. The specimen geometry and boundary conditions for 4-point are shown in (a). An example crack propagation for the case with one compliant inclusion with the total propagation length labeled is shown in (b). Crack propagation for the conjugate case of (b) showing the homogenized area is given in (c).

displacement boundary condition is denoted $\bar{u}_i$. Note that the stress is defined as the derivative of the damaged strain energy density function, $\varphi = ((1-\phi)^2 + k)\psi$. The total (undamaged) elastic energy density is decomposed into 2 parts: the hydrostatic strain energy density (containing only the tensile component)$\psi_I(\varepsilon) = \frac{1}{2}\sum_{k=1}^{n} |\sigma_{kk}\varepsilon_{kk}|^+$, where n is the dimension number, and the deviatoric strain energy density $\psi_{II}(\varepsilon) = \frac{1}{2}|\sigma_{ij}\varepsilon_{ij}|$ with $i \neq j$. The split of the strain energy is to assure a mixed-mode fracture criterion is properly defined. This adaptation is similar to the recent work by Zhang et al. [30] with a difference that a quadratic failure criterion is used instead of the linear one in Zhang et al. [30] (i.e., $\frac{\psi_I(\varepsilon)}{G_{Ic}} + \frac{\psi_{II}(\varepsilon)}{G_{IIc}}$) since the majority of experimental work on mixed-mode fracture in ceramic materials shows a non-linear relation [5,34–36]. We also validated the improved accuracy of this approach in Appendix A.2. Also, it is further assumed that $G_{Ic} = G_{IIc} = G_c$ for a simplified numerical solution.

Due to the addition of ϕ to the degrees of freedom at the nodes, it is difficult to directly use commercial FEM software. In particular, a new element formulation for integrating the phase field parameter, ϕ, using Gauss quadrature is needed. To this end, the phase-field model was implemented in ABAQUS using a user defined element subroutine (UEL). Our implementation follows the approach of Msekh [28]. After implementing the phase-field model within ABAQUS, its accuracy was validated by comparing against two different problems that have exact solutions (discussed in the Appendix A.2).

3. Modeling details

Using the proposed phase-field model, the effect of various composite parameters on crack propagation were simulated including (1) compliant inclusions, (2) stiff inclusions, and (3) hybrid inclusions. The rationale for each composite parameter is outlined below along with the definitions of the metrics used to quantify the effective toughness of the ceramic. To approximate experiments, all test specimens were in a 4-point bending configuration, with a pattern of inclusions introduce near the notch (see Fig. 1). The size of the beam specimen was 10 mm × 110 mm and a precast crack of length 3 mm was located on the symmetry axis along y-direction. The beam was constrained in the x- and y-direction displacements by the pinned connection on the left and in the y-direction by the roller on the right. Loadings were applied in steps with a maximum displacement increment of 10^{-2} mm and a minimum increment of 10^{-6} mm via displacement control within ABAQUS. The pin and roller connections and the two loading points were arranged symmetrically with distances of 50 mm and 25 mm, respectively, to the symmetric axis. Element sizes were no larger than 1/10 of ℓ_0 (defined in

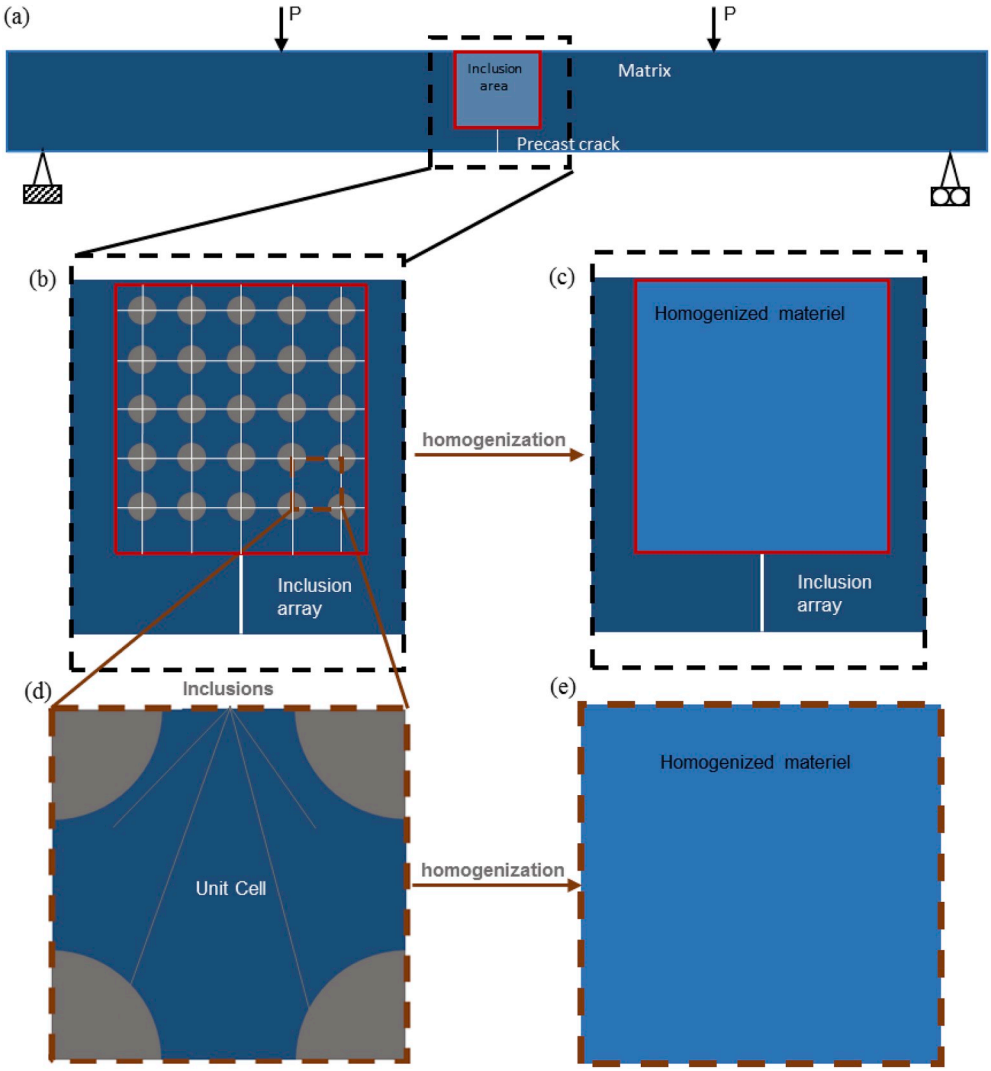

Fig. 3. Homogenization process for determining the effective Young's modulus. The geometry and boundary conditions of the specimen is shown in (a). The homogenization area and partition of unit cells is shown in (b). The total homogenized area is shown in (c). The geometry of a single unit cell is shown in (d). The homogenized are of a single unit cell is shown in €.

Eq. (1)) at the middle span, while an element size of 0.2 mm was used remote from the crack trajectory.

3.1. Inclusion patterns

Inclusions with identical radii were assigned to be within the area shown as light blue in Fig. 1(a). Two series were investigated for compliant inclusions, namely c1 and c2. For the c1 series, 5 columns of compliant inclusions were used with the crack pointing to the middle column, shown in Fig. 1(c). For series c2, 4 columns of compliant inclusions were simulated with the initial crack pointing towards the space between adjacent columns at the middle span of the beam, as shown in

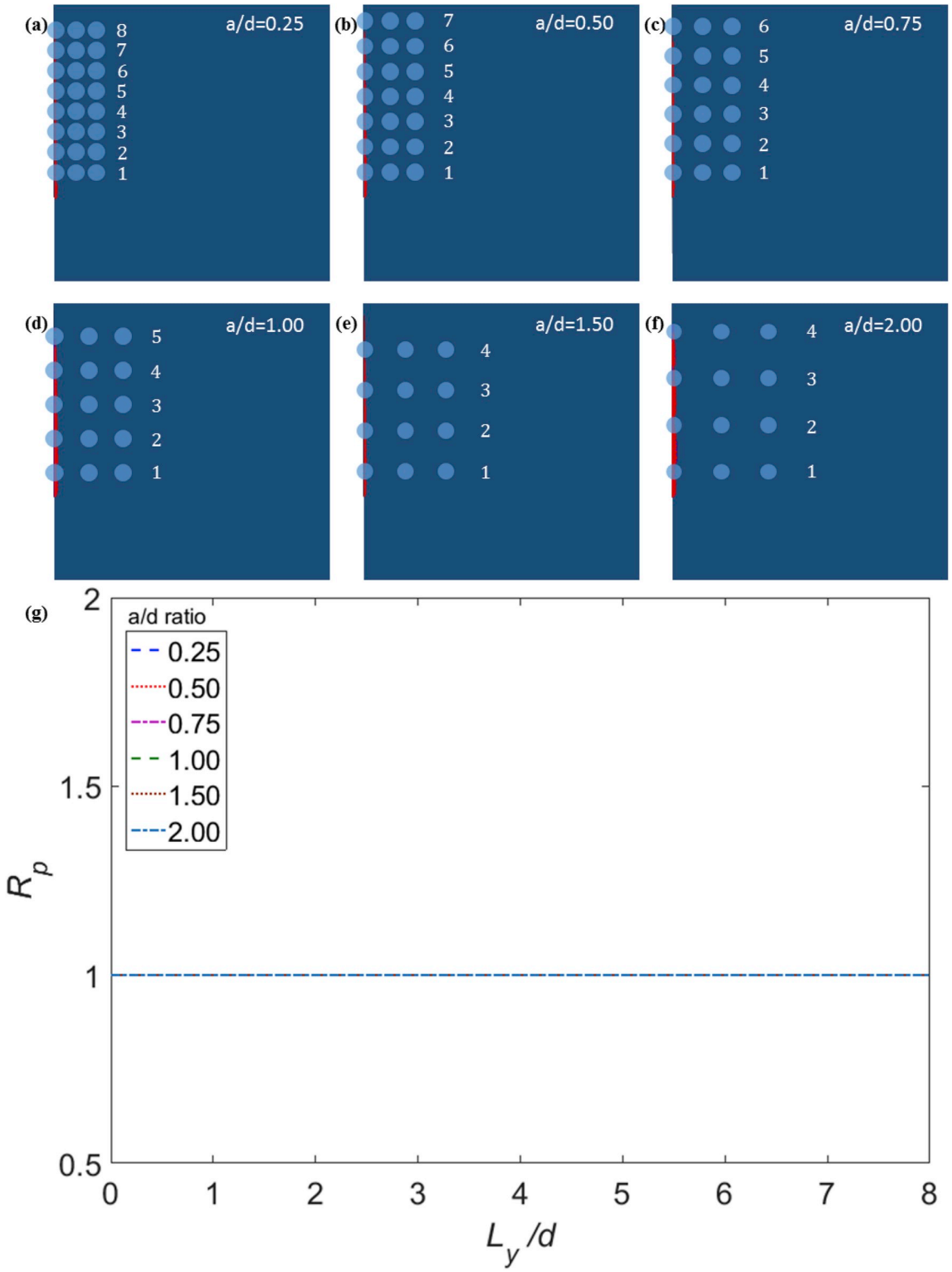

Fig. 4. Crack propagation pattern and propagation ratio for series c1 (rows of inclusions are labeled with numbers on the right side). The crack propagation is illustrated in(a-f) for cases with $a/d = 0.25,\ 0.50,\ 0.75,\ 1.00,\ 1.50,$ and 2.00 , respectively. The propagation ratio, R_p, for each specimen is shown in (g). Note that the curve is identical for each specimen such that the curves lay on top of each other.

Fig. 1(b). Two series were designed to include only stiff inclusions, namely s1 and s2, which had the same geometry as the c2 and c1 series but with stiff inclusions.

Three series were designed to include a hybrid of compliant and stiff inclusions, namely h1, h2, and h3. For the h1 series, 4 columns of inclusions were included with the initial crack pointing towards the space between adjacent compliant and stiff inclusions at the middle span of the beam, as shown in Fig. 1(d), where blue circles represent compliant inclusions and orange ones represent stiff inclusions. For the h2 series, 5 columns were adopted with the initial crack pointing toward the middle column, as shown in Fig. 1(e); thus, the crack is expected to propagate towards compliant inclusion initially. The h3 series has the same geometry as h2 but all the inclusions were altered with the initial crack pointing toward the middle stiff inclusion, such that the stiff inclusions in h2 were replaced with compliant inclusions and vice versa.

For all cases, the inclusion geometries were all set as circles with a fixed diameter of 0.6 mm based on the allowable size in extrusion-based manufacturing methods [37] (denoted as $d = 0.6$ mm and served as the basis for length normalization). The precast crack length was 3 mm (or $5d$) and the distance between crack tip and lowest inclusion row (0.9 mm, or $1.5d$) were fixed for all cases. For each series, the space between nearby inclusions, shown as a in Fig. 1(b–e), was varied to explore the influence of inclusion spacing on the propagation of the crack. It should be noted that the inclusion spacing along the x- and y-directions were set to be identical. Six settings were adopted for each series:$a/d = 0.25$, 0.5, 0.75, 1.00, 1.50, and 2.00. For all series other than h1, half of the specimen was simulated and a symmetry plane is used for computational efficiency.

An alumina matrix (with a Young's modulus of 160 GPa), graphite compliant inclusions (with a Young's modulus of 15.85 GPa), and silicon carbide stiff inclusions (with a Young's modulus of 410 GPa) were selected. The fracture toughness G_c was assumed to be 0.034 N/mm, which is derived from Young's modulus and fracture toughness (K_{IC}) provided by online material property database [38,39], for all materials since the presented work mainly focuses on the effect of elastic mismatch and pattern characteristics. The selection of alumina, graphite, and silicon carbide was due to their wide applications in ceramic composites [40,41].

3.2. Fracture parameters

In order to quantitatively assess and compare the fracture behavior of the various composite arrangements, several metrics are introduced in the following sections. In particular, the propagation ratio, effective Young's modulus, and effective fracture toughness are defined.

3.2.1. Propagation ratio(R_p).

The elongation of the sinuous propagation path is quantified by the propagation ratio,

$$R_p = \frac{L_{prop}}{L_y} \tag{4}$$

where L_{prop} denotes the total length of the propagation path and L_y is the projection of L_{prop} onto the y-axis, and corresponds to the effective propagation path as shown in Fig. 2(b–c). To rule out the influence from the upper boundary, the value of R_p corresponding to $L_y = 8d$ for each case is extracted for comparison. This value is denoted as $R_{p,c}$.

3.2.2. Effective Young's modulus (E_{eff})

The effective Young's modulus is defined for the area containing

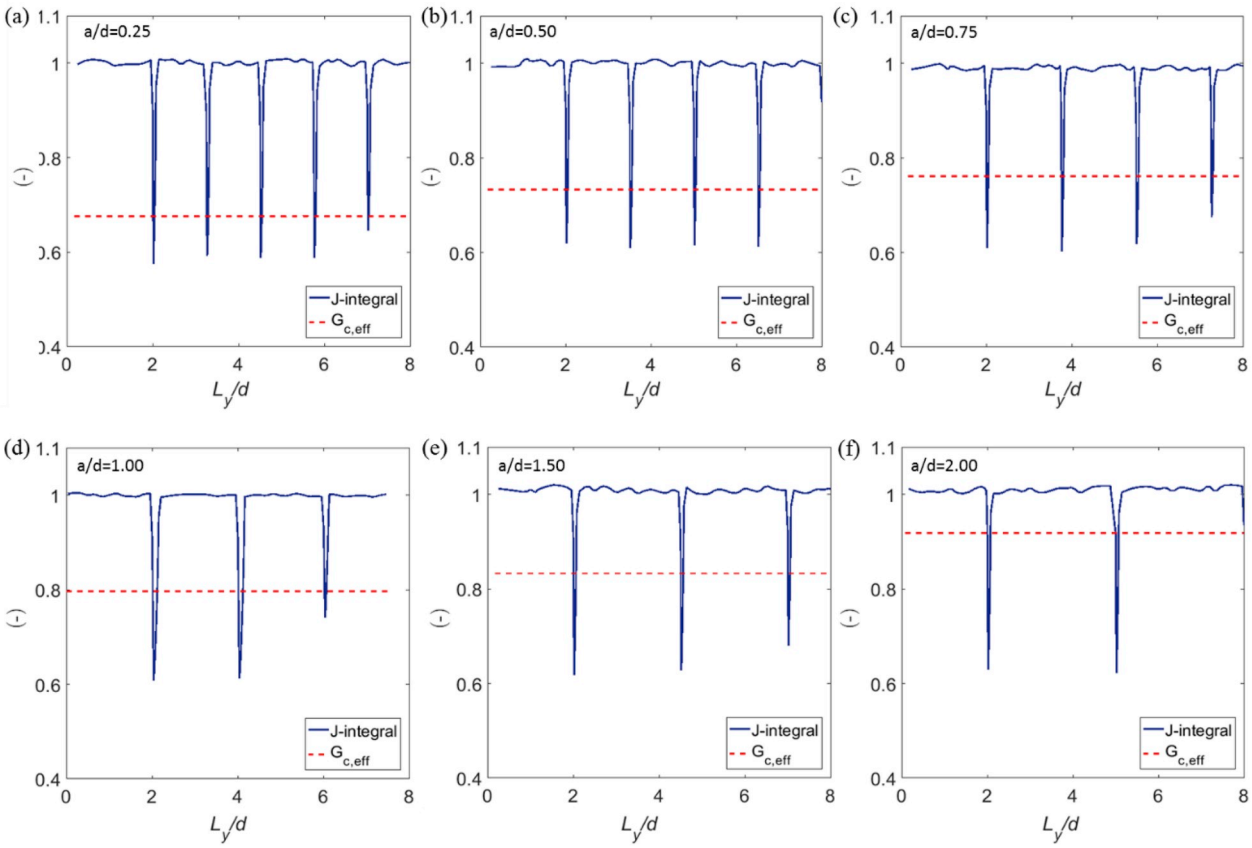

Fig. 5. These plots show normalized J-integral, $\bar{J}$, and effective energy release rate, $G_{c.eff}$, versus relative crack length for series c1 The relative crack length is obtained by normalizing the crack top position by the inclusion diameter, d. Results for specimens with $a/d = 0.25$, 0.50, 0.75, 1.00, 1.50, and 2.00 are shown I (a–f), respectively.

inclusions using the unit cell concept, as shown in Fig. 3(a–c). The unit cell is defined as the area enclosing both the inclusions and matrix, as illustrated in Fig. 3(b, d). Denote $A_{uc,ci}$, $A_{uc,ri}$ $A_{uc,m}$ and A_{uc} as the area of compliant inclusions, stiff inclusions, area of the matrix included in one unit cell, and the total unit cell area, respectively, as shown in Fig. 3(d). Then, the effective Young's modulus is given by

$$E_{eff} = \frac{A_{uc,m}E_m + A_{uc,ci}E_c + A_{uc,ri}E_r}{A_{uc}E_m} \tag{5}$$

where E_c, E_r and E_m are the Young's modulus of the compliant inclusions, stiff inclusions, and matrix, respectively, and can be found in Tab. 1. It should be noted that E_{eff} is a normalized based on E_m.

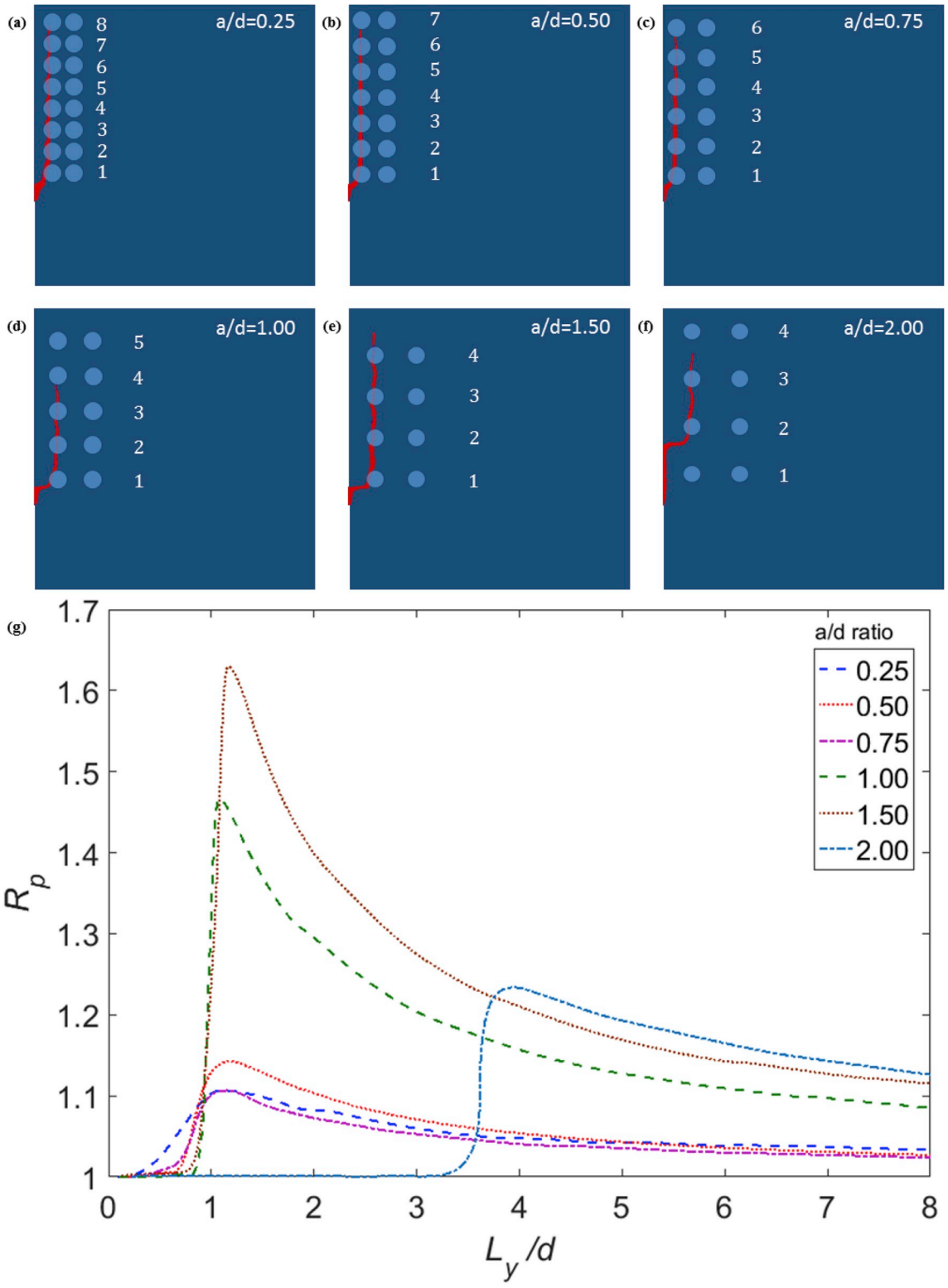

Fig. 6. Crack propagation pattern and propagation ratio for series c2. The crack propagation is illustrated in (a–f) for the cases with $a/d = 0.25, 0.50, 0.75, 1.00, 1.50,$ and 2.00, respectively. Propagation ratio, R_p, versus relative crack length is shown in (g).

3.2.3. Effective fracture toughness ($G_{c,eff}$)

Inspired by the surfing boundary condition in Ref. [7] and considering the geometry of the composite, a homogenization strategy for effective fracture toughness is proposed. A conjugate numerical case is adopted with the effective Young's modulus for the region covering the inclusion patterns. The Young's modulus of the matrix material is used for the area outside. As defined before, L_y is used as the effective crack length for the conjugate numerical case. By applying the same boundary conditions from the original case, the energy release rate can be calculated using LEFM for the conjugate case. The effective fracture toughness was then determined by the energy release rate obtained from the conjugate case during the crack propagation in the original case. The defined effective fracture toughness, $G_{c,eff}$, can then be used to evaluate the effect of inclusion patterns on the fracture resistance.

4. Results and discussions

In this section, the fracture paths, characterized by the propagation ratio, R_p, normalized J-integral for each case (nondimensionalized as $\overline{J} = J/G_c$ with G_c being the critical energy release rate of the matrix and inclusions, cf. Section 3.1), and effective fracture toughness, $G_{c,eff}$, were analyzed to determine the effect of the patterned inclusions on the crack propagation behavior. The fracture trapping, repelling, and guiding mechanisms were observed and discussed in detail.

Organization for this section is as follows: Sections 4.1, 4.2 and 4.3 describe the series of compliant inclusions, stiff inclusions, and hybrid compliant and stiff inclusions, respectively. Section 4.4 summarizes and discusses the mechanisms affecting crack propagation that were observed. For each series, 6 cases with $a/d = 0.25$, 0.50, 0.75, 1.00, 1.50, and 2.00 are labeled as cases *a-f* for sake of brevity. These labels also correspond to the sequence of sub-figures of each series.

4.1. Compliant inclusions

4.1.1. Five inclusion columns (c1)

As shown in Fig. 4(a–f), with the initial crack tip pointing toward the middle column of compliant inclusions, the crack propagates in the *y*-direction without any deviation (regardless of the inclusion spacing). This leads to the fact that the propagation ratio, R_p, remained 1.0 constantly, which can be seen in Fig. 4(g). The crack in Fig. 4 (and subsequent figures) is shown in red, which denotes the area where the damage parameter, ϕ, exceeds the value 0.99, considering the value of ϕ will not reach 1.0 due to the numerical error introduced by parameter k .

As presented in Fig. 5, $\overline{J}$ for all cases fluctuates slightly around the line $\overline{J} = 1.0$ while propagating through the matrix and inclusions. No visible change of $\overline{J}$ is observed when the crack enters each compliant inclusion. However, as the crack propagates into the matrix from the top of each compliant inclusion, $\overline{J}$ decreases rapidly and then returns to 1.0.

4.1.2. Four inclusion columns (c2)

As shown in Fig. 6(a–f), when located around the crack tip, the compliant inclusions tend to attract the crack. For cases *a-e*, the crack propagates at first along the *y*-direction for a very short distance before turning towards the compliant inclusion of the 1st row. Subsequently, the crack propagates along one column of inclusions in the *y*-direction. As for case *f*, the crack propagates following the initial direction until it gets close to the 2nd row of inclusions. This is due to the fact that with this relative inclusion spacing ($a/d = 2$), the 1st row of inclusions is not sufficiently close to the initial crack tip to alter the propagation path. Thus, it can be observed that for a fixed set of materials, there exists an

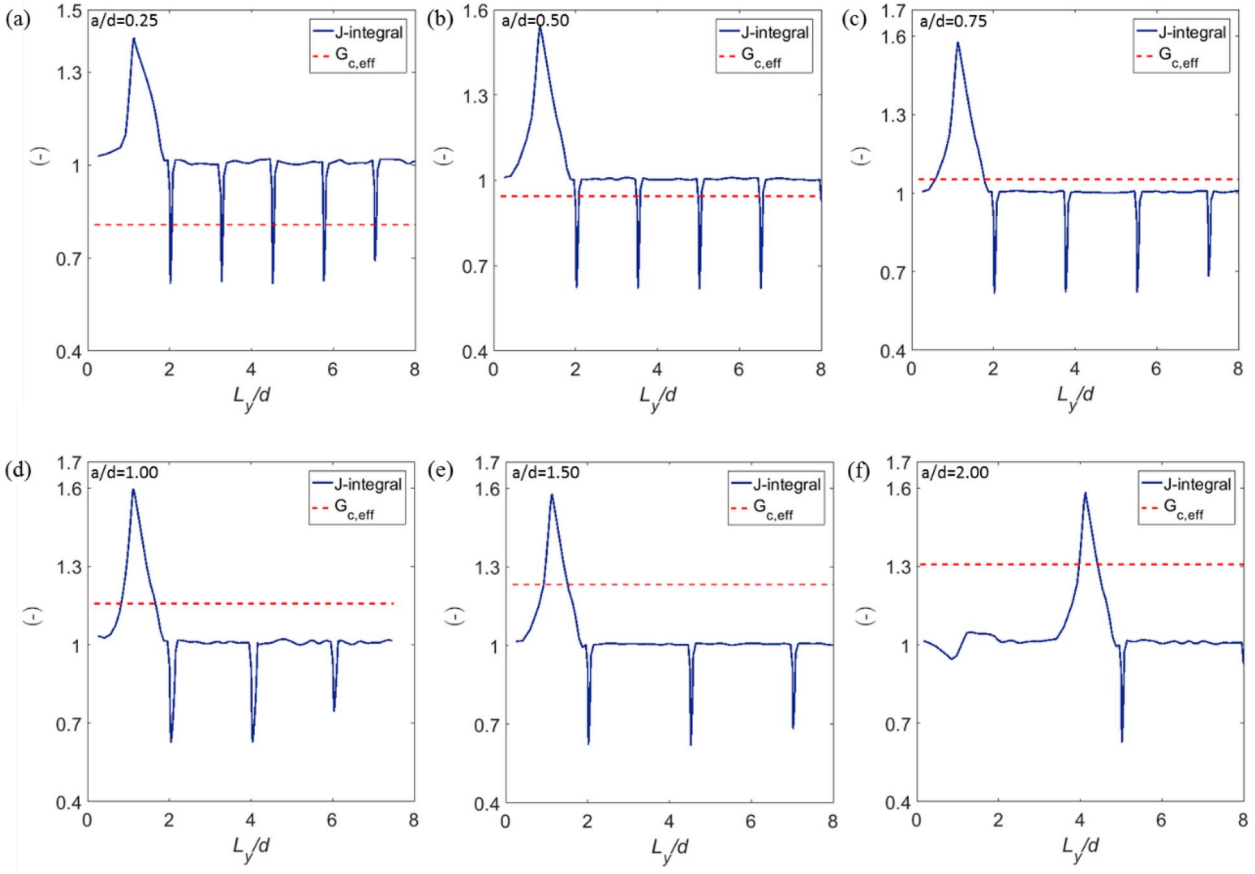

Fig. 7. These plots show normalized J-integral, $\overline{J}$, and effective energy release rate, $G_{c,eff}$, versus relative crack length for series c2. Results for specimens with $a/d = 0.25$, 0.50, 0.75, 1.00, 1.50, and 2.00 are shown in (a–f), respectively.

optimum inclusion spacing that results in the greatest increase in crack length.

As shown in Fig. 7, a relatively large jump in $\overline{J}$ within the crack position range of 0 to 1 mm was observed for cases *a-e*. This jump corresponds to the crack propagating towards the inclusions of the 1st row. This behavior was also observed for case *f* when the crack tip reached the inclusions at the 2nd row, and coincided with the increasing R_p, as shown in Fig. 6(g). These results indicate that the crack-trapping mechanism can be introduced by placing the compliant inclusion at a limited distance away from the crack tip. The increased fracture path provides more release of fracture energy hence increasing the effective fracture toughness.

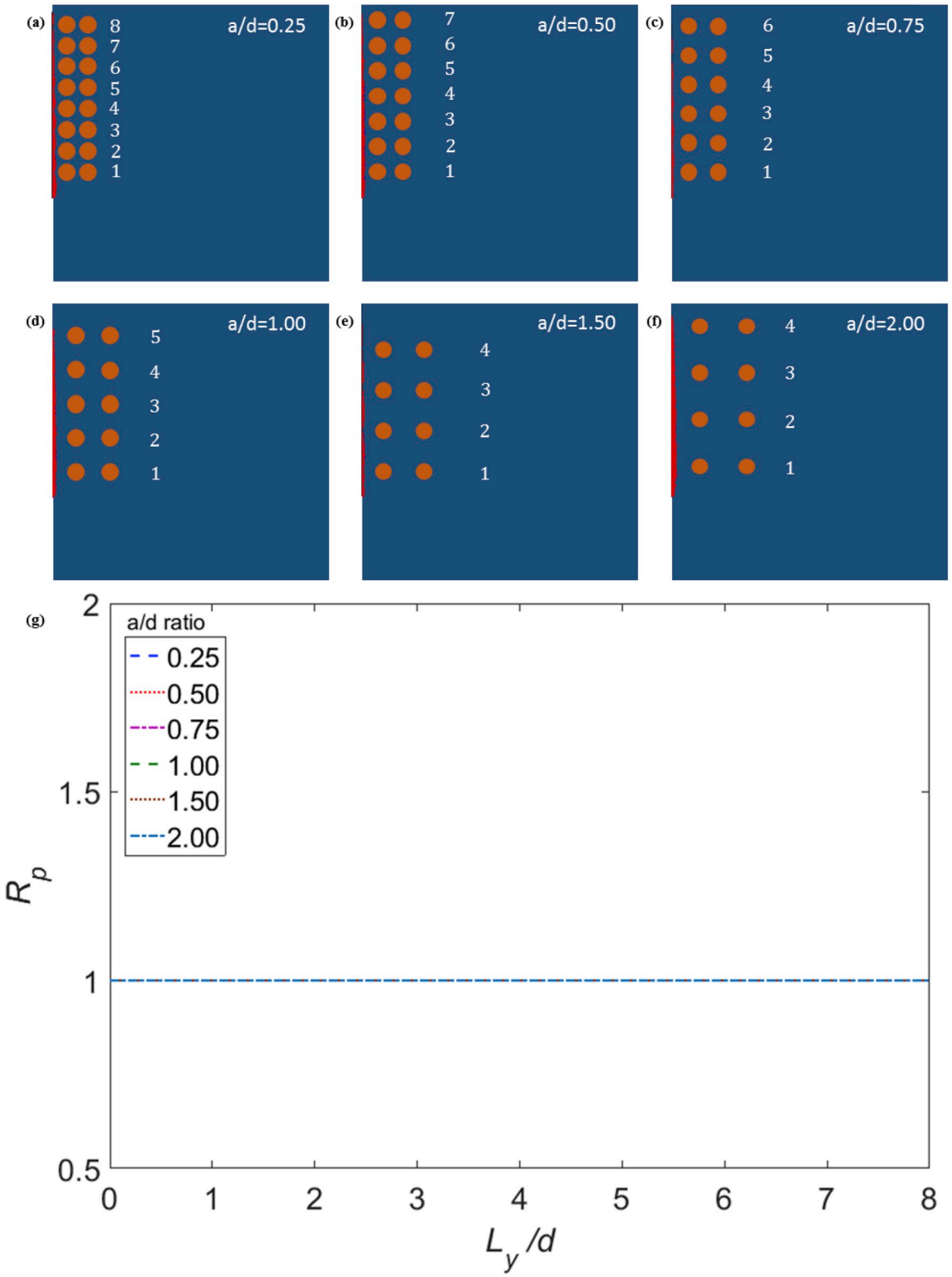

Fig. 8. Crack propagation pattern and propagation ratio for series s1. (a–f). The crack propagation is illustrated in (a–f) for cases with $a/d = 0.25$, 0.50, 0.75, 1.00, 1.50, and 2.00, respectively. The propagation ratio, R_p, versus relative crack length for each specimen is shown in (g). As in Fig. 4, the curves for each specimen are identical and lay on top of each other.

4.2. Stiff inclusions

4.2.1. Four inclusion columns (s1)

As shown in Fig. 8(a–f), with stiff inclusions distributed symmetrically about the initial crack, the crack propagates in the *y*-direction with a constant propagation ratio, $R_p = 1$, as shown in Fig. 8(g). As shown in Fig. 9, although the propagation pattern for this scenario is no different than homogeneous situation or series c1, $\overline{J}$ shows periodic fluctuations, indicating the influence of nearby stiff inclusions. The number of fluctuations, corresponding to the number of inclusions within the area, decreased from 6 to 2 when the number of rows decreased from 8 to 4. The amplitude of the fluctuations, corresponding to the inclusion spacing, decreased from around 0.25 to 0.05 when a/d increased from 0.25 to 2, which shows that the influence of stiff inclusions is reduced as the spacing between the stiff inclusions and crack tip is increased.

4.2.2. Five inclusion columns (s2)

As shown in Fig. 10(a–f), stiff inclusions can change the fracture propagation path by repelling the crack tip away from the inclusion. The overall propagation process can be divided into two stages: (1) straight crack growth due to the initial crack direction and then an altering process while reaching the stiff inclusions of the 1st row followed by a stage (2) where crack propagation is constrained between two columns of stiff inclusions.

As shown in Fig. 11, corresponding to the two-stage propagation, the value of $\overline{J}$ also exhibits two stages: (1) an initial fluctuation within the crack position range of 0 to 0.8 mm reflecting the initial large crack deflection process. The amplitude of the initial fluctuation decreases slightly with increasing inclusion spacing, which is due to the fact that as the inclusion spacing increases, the crack has more space between the adjacent columns of inclusions to propagate at will. As for the steady propagation stage (2), a periodic fluctuation is observed. With increasing inclusion separation, the amplitude of the fluctuation does not change significantly, but the average value increases gradually due to the increasing inclination angle of the crack. Series s2 shows the strong crack repelling mechanism of using stiff inclusions, in which the crack was always deflected away from the inclusions. This observation is consistent with the trend of R_p, as shown in Fig. 10(g).

4.3. Hybrid stiff and compliant inclusions

4.3.1. Four inclusion columns (h1)

As shown in Fig. 12(a–f), the crack propagation pattern varies significantly with increasing a/*d*. For cases *a-b*, the crack propagates mainly along a zigzag route after initiation, i.e., the path connects compliant inclusions for each row in sequence. Also, it can be observed that branches emerge while propagating towards stiff inclusions. After branching, the crack further develops along one of the branches and marches towards the compliant inclusion.

As a/d increases more for cases *c-d*, where a/d reaches the value of 0.75 and 1.00 separately, the crack chooses a path periodically crossing compliant inclusions and bypassing stiff inclusions of the same column. Small branches are observed to initiate and arrest immediately after.

For an even higher $a/d = 1.50$ in case *e*, two major branches are observed after the crack initiation. The left branch grows towards the compliant inclusion of the 2nd row and the right branch grows towards the compliant inclusion of the 1st row. When the loading process continues on, the right branch arrests while reaching the 2nd row and the left branch continues propagating with the latter part exhibiting a similar pattern with cases *c-d*: crossing compliant inclusions and

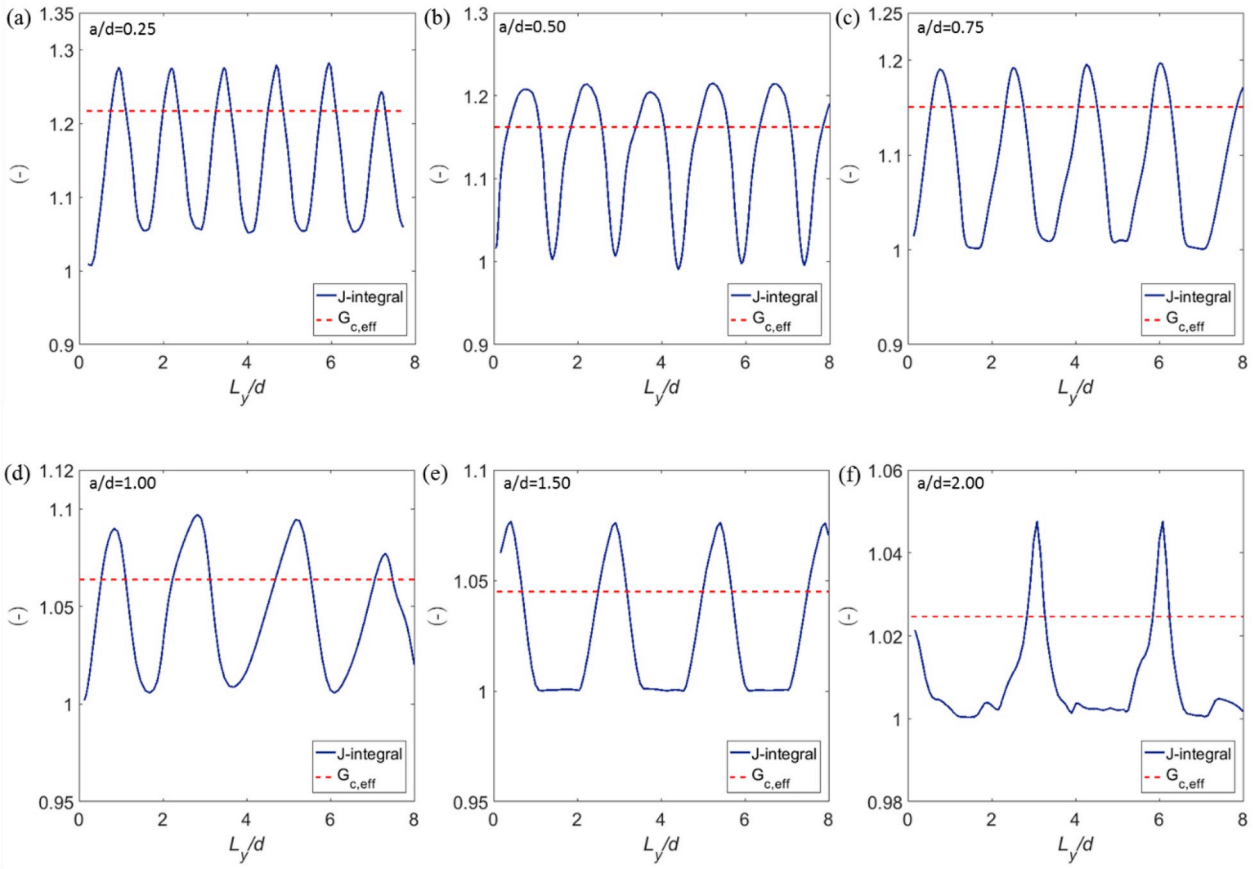

Fig. 9. These plots show normalized J-integral, $\overline{J}$, and effective energy release rate, $G_{c,eff}$, versus relative crack length for series s1. Results for cases with $a/d = 0.25$, 0.50, 0.75, 1.00, 1.50, and 2.00 are shown in (a–f), respectively.

bypassing stiff ones.

For case *f* with the maximum $a/d = 2.00$, the crack propagates in the *y*-direction before deflecting towards and entering the compliant inclusion of the 2nd row. Small branches are also observed. However, further growth was not observed for these small branches. The subsequent propagation exhibited similar behavior to cases *c-d*: entering compliant inclusions and bypassing stiff ones. Branches were also observed at each row.

As shown in Fig. 12(g), the propagation ratio, R_p, corresponding to the longest final propagation path with $a/d = 0.25$ and 0.5 is much larger than the other cases, which is due to the multiple branches and zigzag route. Cases with inclusion spacing of $a/d = 1.00$ resulted in the lowest value of R_p due to minimal deflections and branches.

As shown in Fig. 13, the behavior of $\overline{J}$ is similar to that of the specimens described before. For cases *a-b*, $\overline{J}$ decreases rapidly when the crack propagates from a compliant inclusion into the matrix and then increases and reaches a relatively high value due to the branching and inclination angle. This behavior repeats when the crack crosses compliant inclusions in the first 5 rows. The higher value of $\overline{J}$ seen in case *b* is due to the developments of more branches. For cases *c-f*, $\overline{J}$ decreases when the crack passes through the boundaries from the inclusion side into the matrix, and then increases while the crack bypasses the following stiff inclusion until reaching the top surface.

4.3.2. *Five inclusion columns: precast crack pointing to compliant inclusion (h2)*

As shown in Fig. 14(a–f), the crack propagates through the nearest compliant inclusion after the crack initiation for all cases, and then the patterns vary for increasing inclusion spacing in a similar fashion as series h1. For cases *a-b*, branches are observed as the crack propagates past the compliant inclusion of the 2nd row. The right branch enters the rightmost compliant inclusion of the 3rd row and then arrests, while the left branch propagates between compliant inclusions of the subsequent rows. For cases *c-f*, the crack only enters the compliant inclusions in the middle column. Instead of choosing a route connecting compliant inclusions for each row, the crack propagates periodically entering the

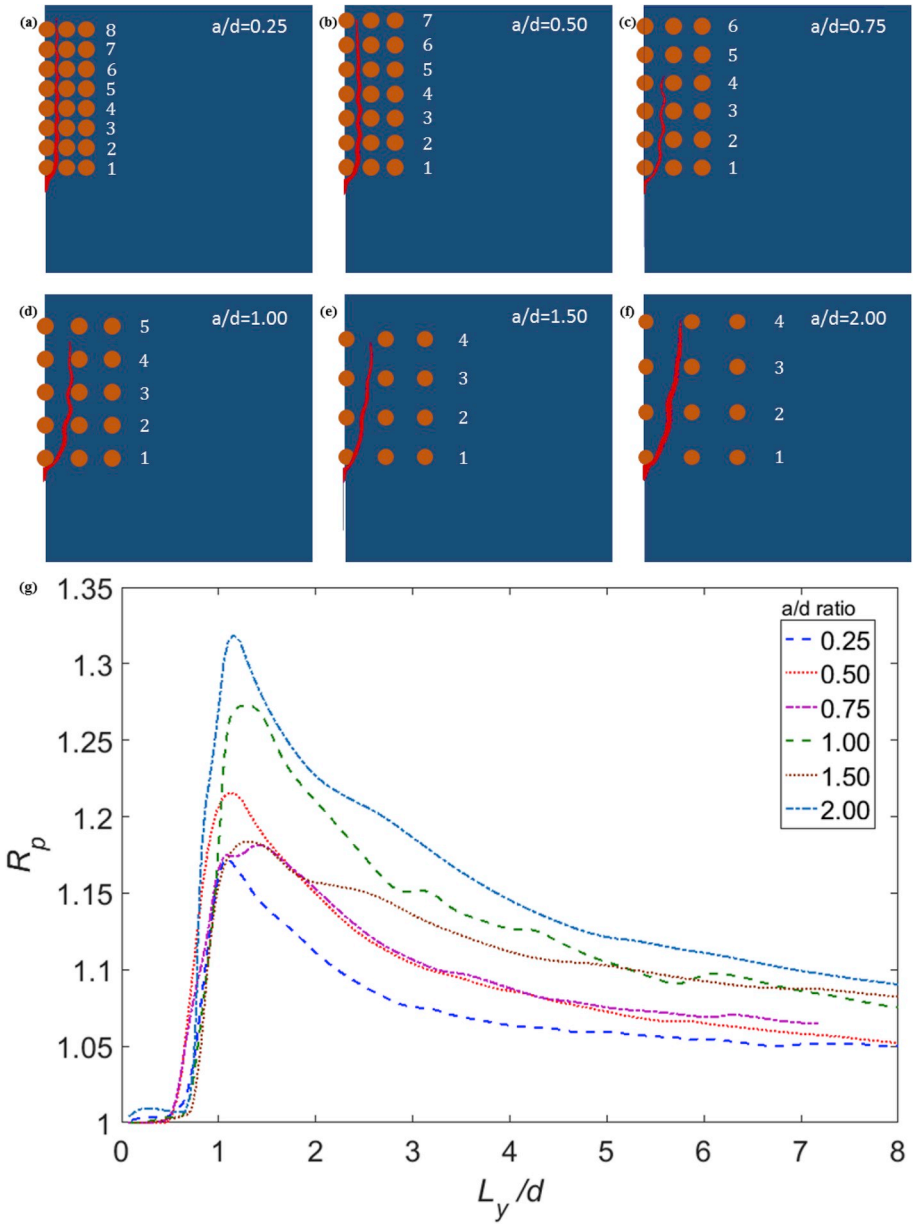

Fig. 10. Crack propagation pattern and propagation ratio for series s2. The crack propagation is illustrated for cases with $a/d = 0.25$, 0.50, 0.75, 1.00, 1.50, and 2.00 in (a–f), respectively. The propagation ratio, R_p, versus relative crack length is shown in (g).

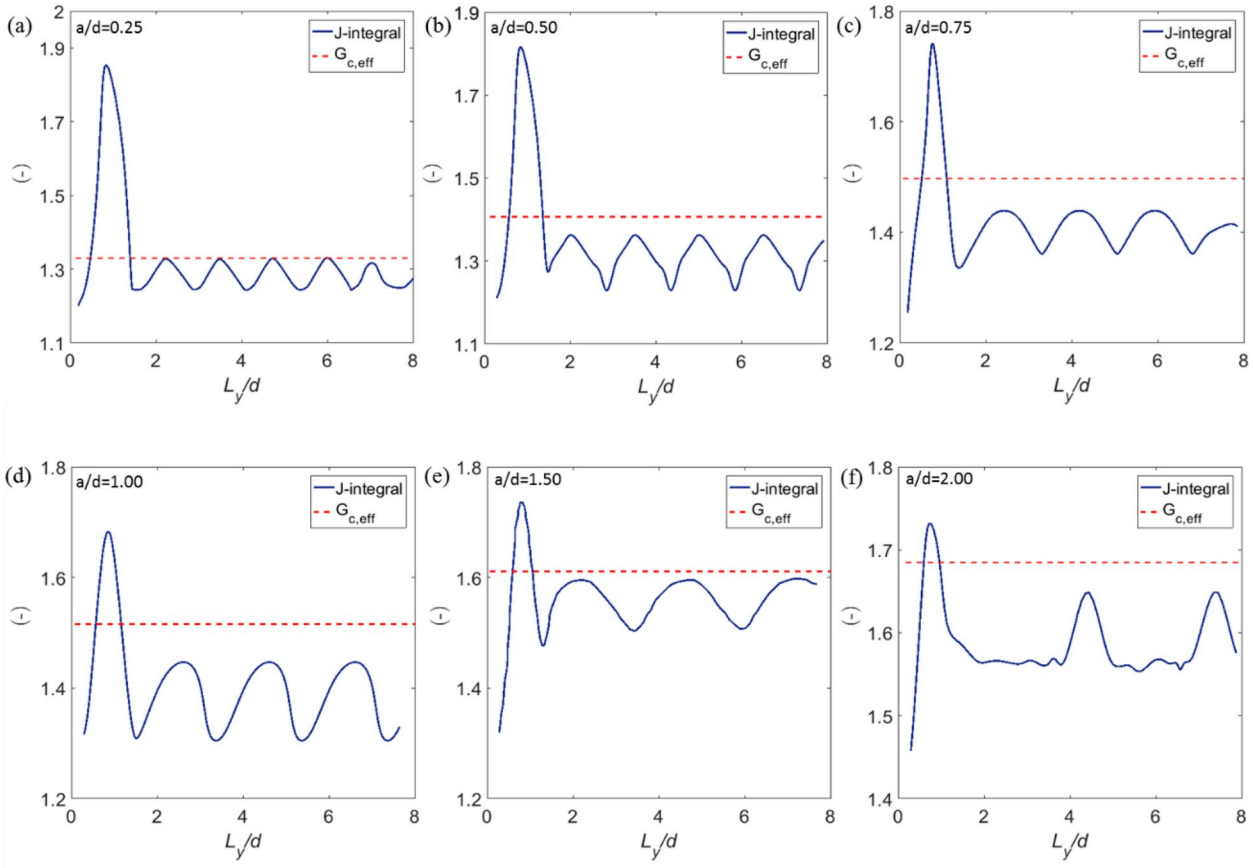

Fig. 11. These plots show normalized J-integral, $\overline{J}$, and effective energy release rate, $G_{c,eff}$, versus relative crack length for series s2. Results for cases with $a/d = 0.25$, 0.50, 0.75, 1.00, 1.50, and 2.00 are shown in (a–f), respectively.

compliant inclusions and bypassing the stiff inclusions within the same column. Similarly, as observed in series h1, the final propagation ratio, R_p, of cases *a-b* is much longer than that of cases *c-f*.

As seen from Fig. 15, the behavior of $\overline{J}$ is similar to series h1. The increasing of $\overline{J}$ arises mainly from the inclination and branching effects, which also explains the remarkably higher peak compared with the cases shown in Fig. 15(c–f). The periodicity of $\overline{J}$ corresponds to that of R_p, as shown in Fig. 14(g).

4.3.3. Five inclusion columns: initial crack pointing to a stiff inclusion (h3)

A similar crack behavior as series h2 was observed, as shown in Fig. 16. For cases *a-b*, after initiation, the crack bypasses the stiff inclusion and then enters the compliant inclusion of the 1st row. Crack branching was been observed while the crack propagated through the compliant inclusions. The crack propagation in cases *c-d* followed a similar behavior to cases *c-d* of series h2: propagating periodically bypassing the stiff inclusions and crossing the compliant inclusions. In Fig. 17, when the inclusions are arranged in an opposite fashion to the corresponding cases with same a/d ratio of series h2, the same fracture behavior can be observed - aside from higher peaks due to the increased number of crack branches.

All the cases with hybrid compliant and stiff inclusions (h1, h2, and h3) reveal a crack guiding and controlling mechanism. A smaller inclusion spacing (i.e., smaller a/d) provides increased control of the crack path by forcing the crack to grow along a zig-zag connecting compliant inclusions and avoiding stiff inclusions. The smaller inclusion spacing also reduces the occurrence of crack branching which makes the crack growth more predictable. For larger inclusion spacing, the attraction and repelling effects of compliant and stiff inclusions are reduced. Thus, the crack propagates periodically crossing compliant inclusions and bypassing stiff ones of the same column. It can be seen in this design, that the effective toughness can be increased by hybrid inclusions and changing the inclusion spacing.

4.4. Toughening mechanisms

4.4.1. Crack trapping with compliant inclusions

First, as can be seen from E_{eff} shown in Fig. 18(a), the pure compliant inclusions of series c1 and c2 had a pure reducing effect on the overall effective Young's modulus.

Considering the fact that the propagation path was not affected by the compliant inclusions in the c1 series, as shown in Fig. 18(b), the corresponding $G_{c,eff}$ showed only the effect from the material property mismatch introduced by the compliant inclusions. As presented in Fig. 18(d), $G_{c,eff}$ of series c1 is nearly linearly related to the E_{eff}, which means a higher inclusion spacing leads to a higher E_{eff}, as well as a higher $G_{c,eff}$. It should be noted that the maximum $G_{c,eff}$ is less than one, which means that while the propagation path was unchanged, compliant inclusions reduced the overall fracture resistance.

As for series c2, the overall effective Young's modulus, denoted by E_{eff}, was still the same with series c1. However, the attraction effect of compliant inclusions led to an altered crack propagation path, and thus the total propagation path was elongated, as shown in Fig. 18(b), and the effective energy release rate, $G_{c,eff}$, was increased. The effect of a longer total propagation distance, L_{prop}, which led to higher fracture energy, counteracted the reducing effect of the compliant inclusions, which explains the reason why values of the effective energy release rate, $G_{c,eff}$, for the cases shown in Fig. 7(c–f), are greater than one.

Overall, the fracture resistance property, $G_{c,eff}$, is affected by both the elastic mismatch and a/d ratio for patterned compliant inclusions. The

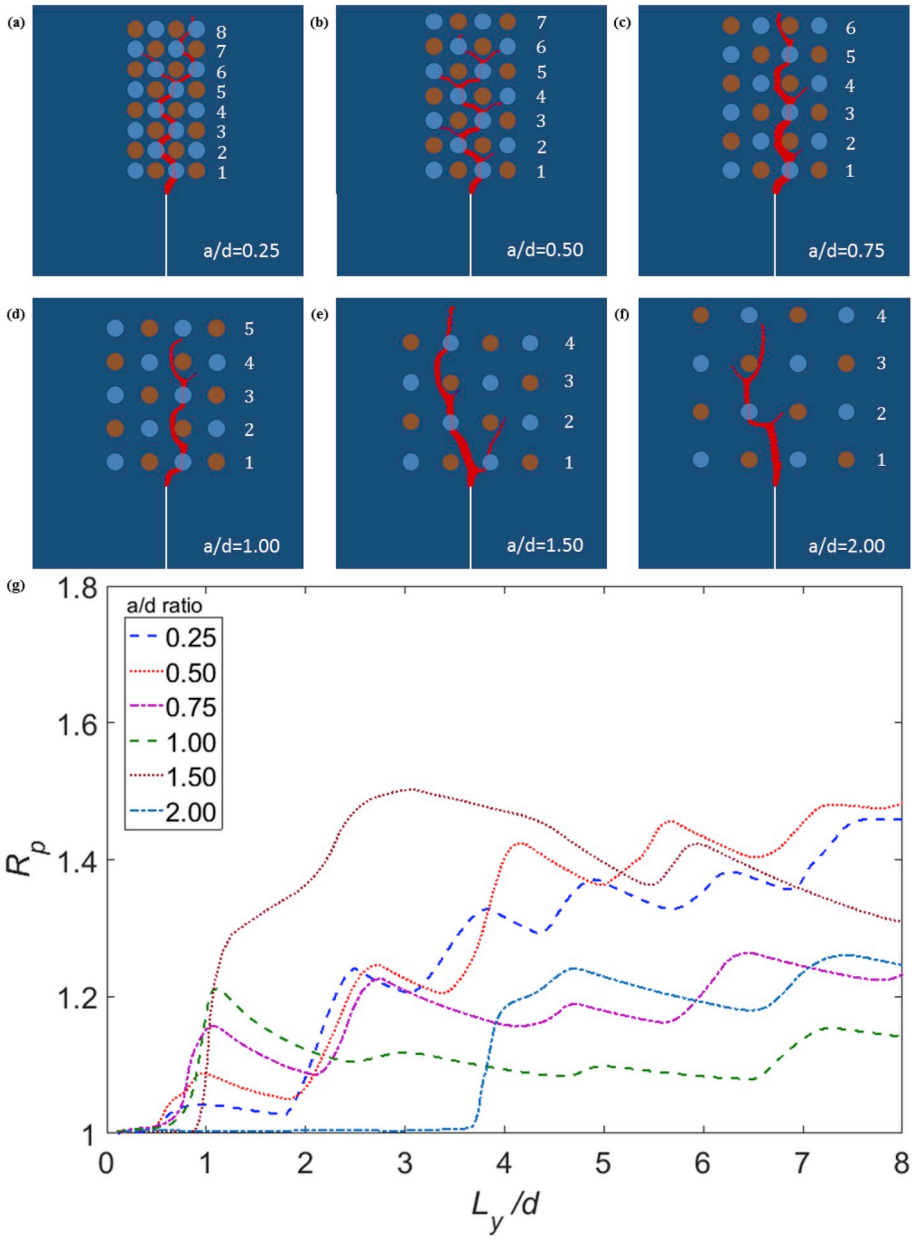

Fig. 12. Crack propagation pattern and propagation ratio for series h1. The crack propagation is illustrated for cases with $a/d = 0.25$, 0.50, 0.75, 1.00, 1.50, and 2.00 in (a–f), respectively. The propagation ratio, R_p, versus relative crack length is shown in (g).

underlying crack trapping mechanisms were observed and also explained analytically for a local setting in our recent work [37]. The lower Young's modulus of the compliant inclusion can create a low local stress field and large strain field which leads the crack propagation towards the inclusion. However, these local fields become less effective when the inclusions are farther away from the crack tip. Therefore, it is possible to use compliant inclusions to trap the crack as observed from the computational results. However, this effect is very limited when a/d exceedingly large.

4.4.2. Crack repelling with stiff inclusions

As can be seen from E_{eff} shown in Fig. 18(a), the pure stiff inclusions of series s1 and s2 has a pure enhancing effect on the overall effective Young's modulus.

While the propagation path was not changed throughout series s1 due to the symmetric arrangement of stiff inclusions, as shown in Fig. 18 (b), the effective energy release rate, $G_{c,eff}$, of all the cases in this series was greater than one, which indicates that the stiff inclusions near the crack path enhanced the fracture toughness. Similarly, as explained for the trapping mechanism, the stiff inclusions induce a compressive local stress field which tended to close the crack tip when propagating. It was also observed that with increasing inclusion spacing, the effective energy release rate, $G_{c,eff}$, of series s1 decreased, which indicates that the enhancing effect reduces when the inclusions are farther apart.

When the propagation path is altered, as shown in Fig. 18(b), results from series s2 showed that the a/d ratio also affects the fracture resistance via the repelling mechanism, and thus leads to a longer total propagation distance, L_{prop}. This also resulted in a higher effective energy release rate. The change in energy release rate, $G_{c,eff}$, with inclusion spacing and effective Young's modulus, E_{eff}, can be found in Fig. 18 (c–d). It should be noted that although the effective Young's modulus is decreasing with increasing interspacing, a, the increasing $R_{p,c}$ reflects a larger propagation distance and leads to an increasing $G_{c,eff}$. This means that increasing the propagation distance has a more significant effect on

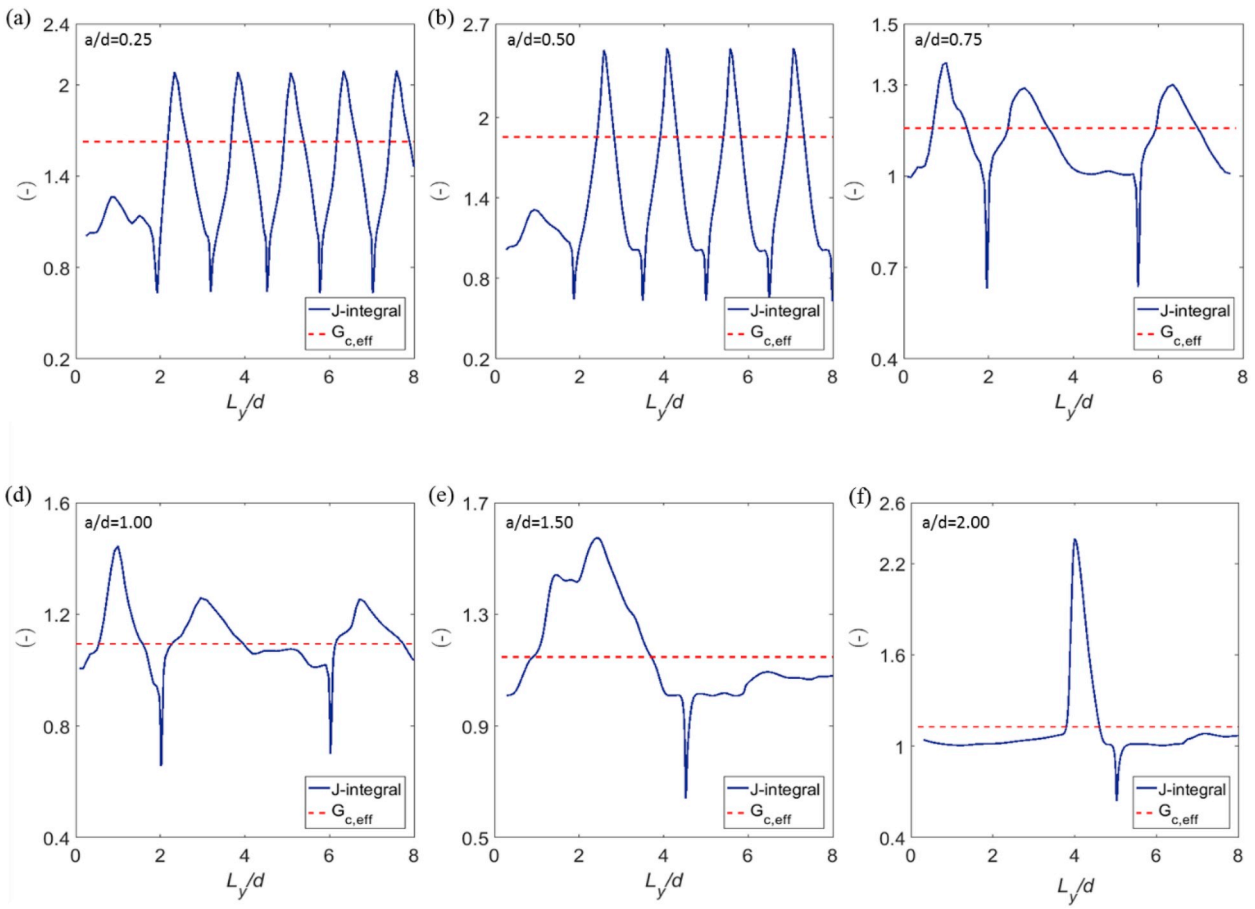

Fig. 13. These plots show normalized J-integral, $\overline{J}$, and effective energy release rate, $G_{c,eff}$, versus relative crack length for series h1. Results for cases with $a/d =$ 0.25, 0.50, 0.75, 1.00, 1.50, and 2.00 are shown in (a–f), respectively.

$G_{c,eff}$ than elastic mismatch.

In addition, the results of the c1 and s1 series, as seen in Fig. 18(d), showed that elastic mismatch has a significant effect on effective energy release rate with a straight crack path. Alternatively, with the crack trapping mechanism from the compliant inclusions and repelling effect of the stiff inclusions introduced into the system, the altered propagation path increased the overall effective energy release rate by increasing the total propagation distance.

4.4.3. Crack guiding with hybrid inclusions

For the series with hybrid compliant and stiff inclusions, the effective Young's modulus decreases slightly with increasing inclusion spacing compared to pure compliant or stiff inclusion series. The corresponding effective energy release rate was mainly influenced by the inclusion spacing.

It can be concluded from series h1, h2 and h3, that the hybrid arrangements of compliant and stiff inclusions lead to a zigzag crack propagation mode when the inclusion spacing was sufficiently small. Thus a longer propagation path is reached and resulted in a higher overall fracture resistance. As shown in Fig. 19(c–d), with more branches and inclinations, the effective energy release rate for cases *a-b* with $a/d = 0.25$ and 0.5 were higher than that of the cases with higher a/d ratios, which shared same trend with $R_{p,c}$. A maximum in the effective energy release rate appeared when $a = 0.50d$. For higher inclusion spacing, the combination of attraction effects of compliant inclusions and repelling effects of stiff inclusions is not sufficient to significantly alter the crack path resulting in a much lower $R_{p,c}$. Results of these three series show the possibility of manipulating the crack propagation path using the patterned hybrid inclusions for ceramic composites. A alternating arrangement of compliant and stiff inclusions with proper spacing could significantly increase the overall toughness and provide a means to guide crack propagation.

4.4.4. Crack branching

Crack branching was observed when the crack propagated toward stiff inclusions. The repelling effect due to local compressive stresses forced the crack tip to bifurcate forming the branched cracks as shown in Figs. 12, 14 and 16. This crack tip bifurcation originates from the symmetric condition with respect to the crack path which typically are along the radial direction running towards the stiff inclusions. This branching is mainly caused by the local stress field. However, this may be slightly different from the actual experiment where local defects may disturb the stress distribution at the crack tip. Sufficive to say, the numerical results confirm the fact that additional cracks can possibly be generated via branching due to the combination of compliant and stiff inclusions.

5. Conclusion

In this work, a mixed-mode phase-field model was proposed and implemented to investigate the effect of compliant and stiff inclusions on the fracture resistance properties of 4-point bending beam specimens. The crack trapping, repelling, and guiding mechanisms were observed for different patterns. The effects of these mechanisms on the fracture behavior of the composites were characterized. The following conclusions can be drawn:

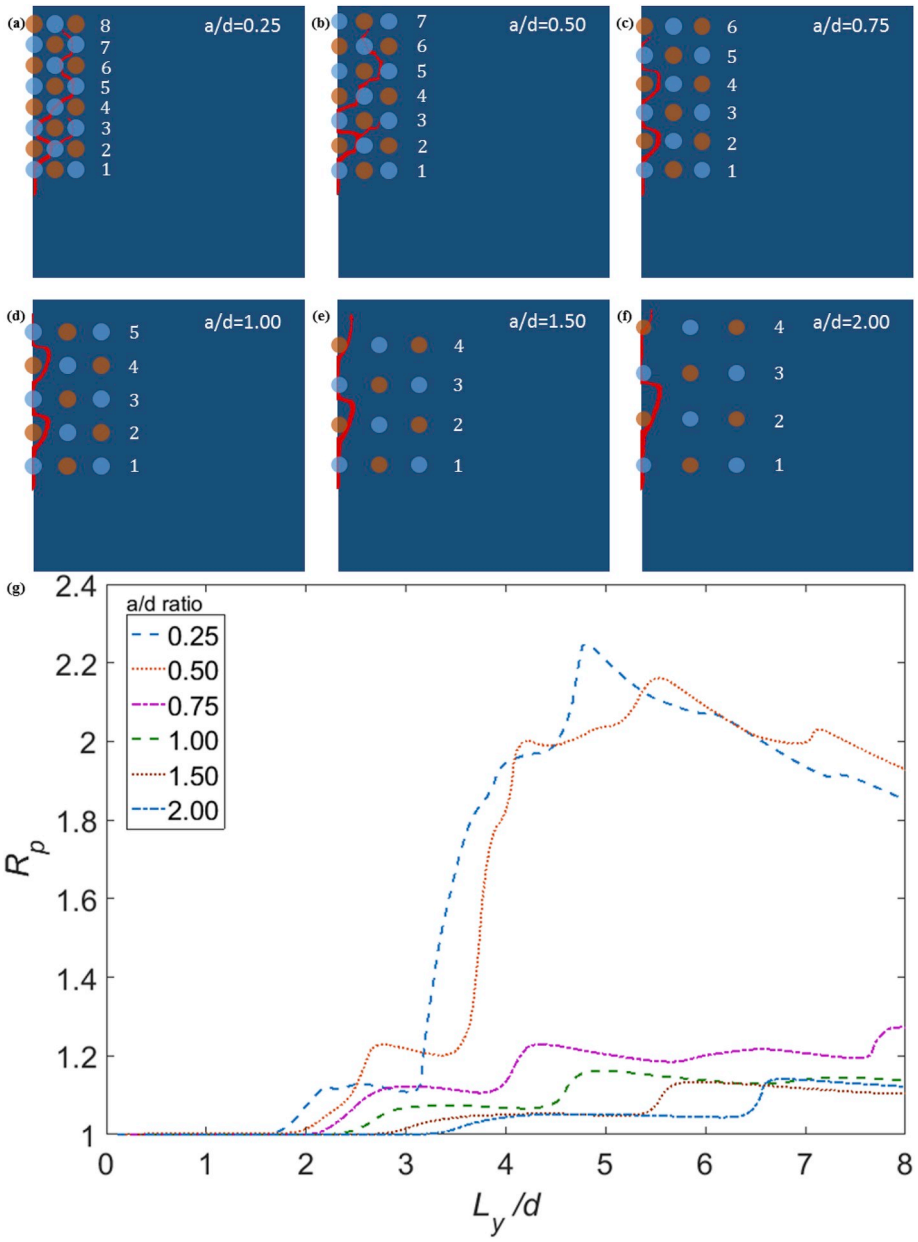

Fig. 14. Crack propagation pattern and propagation ratio for series h2. The crack propagation is illustrated for cases with $a/d = 0.25$, 0.50, 0.75, 1.00, 1.50, and 2.00 in (a–f), respectively. The propagation ratio, R_p, versus relative crack length is shown in (g).

(1) If the propagation route follows the direction of the initial crack, the presence of compliant inclusions reduces the fracture resistance of the composite, as shown in the results of series c1. The degree of reduction is approximately linear to the volume fraction of the compliant inclusions. On the other end, the presence of stiff inclusions would have an enhancing effect on the fracture resistance property, as shown in results of series s1.
(2) Results of series c2 show that the compliant inclusion can trap the crack tip when arranged closely together. By comparison, the stiff inclusions deflect or repel crack propagation, as shown in series s2. In both ways, the crack route is altered and the fracture resistance is increased.
(3) With the combination of compliant and stiff inclusions, the total propagation distance can be significantly increased compared to cases with only compliant or stiff inclusions. As shown in cases *a-b* of series h1, h2, and h3, the crack follows a zigzag route connecting compliant inclusions of rows in sequence. Crack branching is also introduced to the system, which increases the effective energy release rate as much as 4.53 times that in the homogeneous case. This enhancement is found to be the most significant for inclusion spacing within the range $0.25 < a/d < 0.75$.

In summary, the combination of the compliant and stiff inclusions with an arrayed pattern was able to control and guide the fracture propagation to enhance the effective fracture toughness of the ceramic composite. The enhancement is closely related to the elastic mismatch between the inclusion and matrix and is constrained by the ratio of inclusion spacing to inclusion size for the composites. This result demonstrates a new approach for designing ceramic composites to optimize fracture resistance using patterned inclusions. The concept can be applied using various additive manufacturing techniques including 3D printing and co-extrusion sintering.

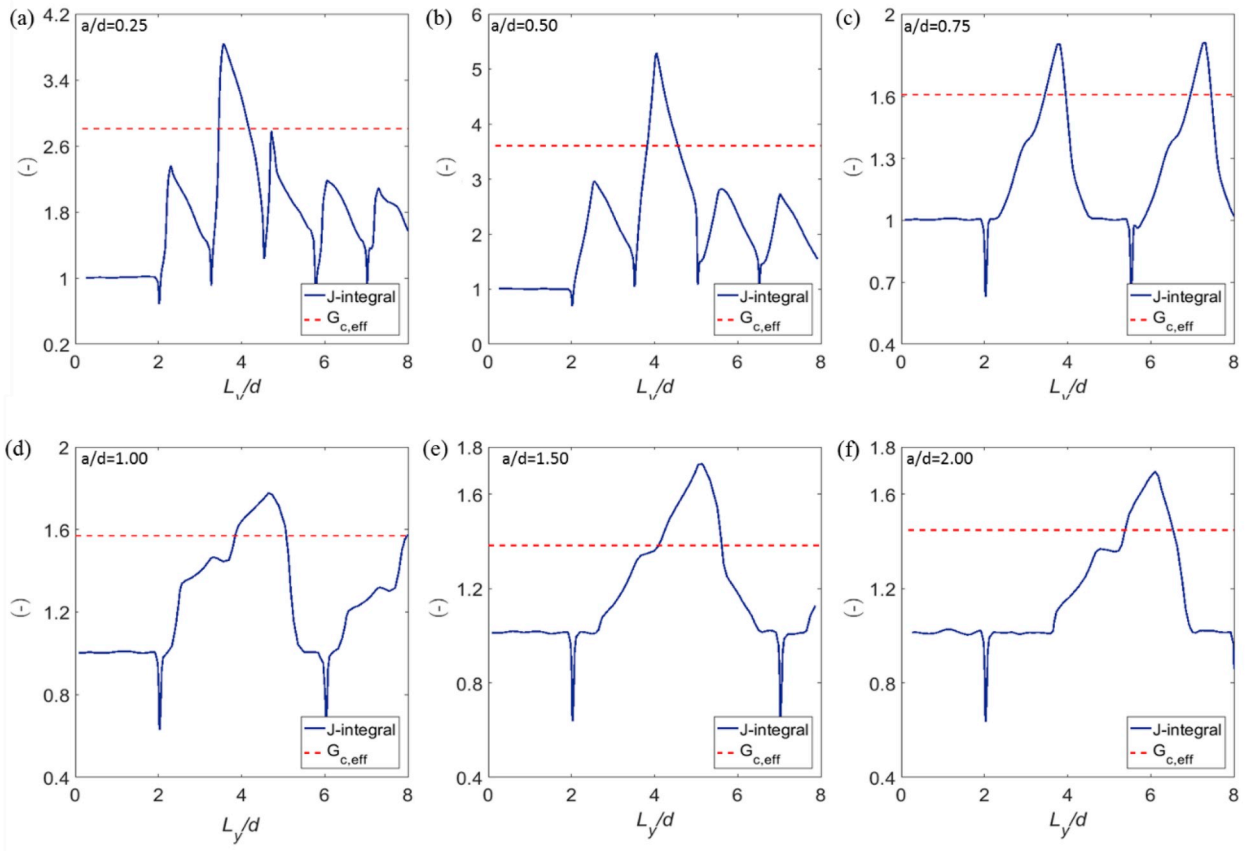

Fig. 15. These plots show normalized J-integral, $\overline{J}$, and effective energy release rate, $G_{c,eff}$, versus relative crack length for series h2. Results for cases with $a/d =$ 0.25, 0.50, 0.75, 1.00, 1.50, and 2.00 are shown in (a–f), respectively.

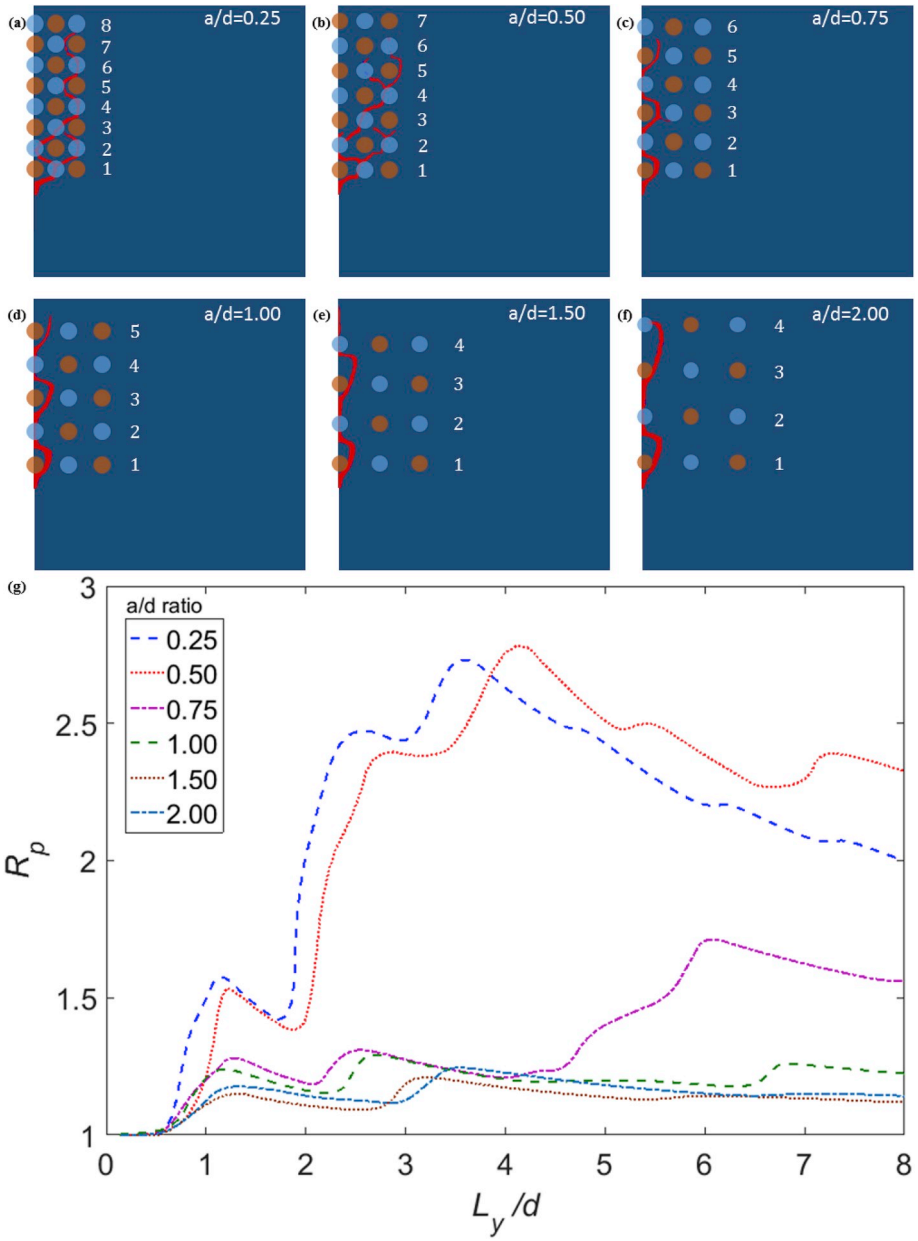

Fig. 16. Crack propagation pattern and propagation ratio for series h3. The crack propagation is illustrated for cases with $a/d = 0.25$, 0.50, 0.75, 1.00, 1.50, and 2.00 in (a–f), respectively. The propagation ratio, R_p, versus relative crack length is shown in (g).

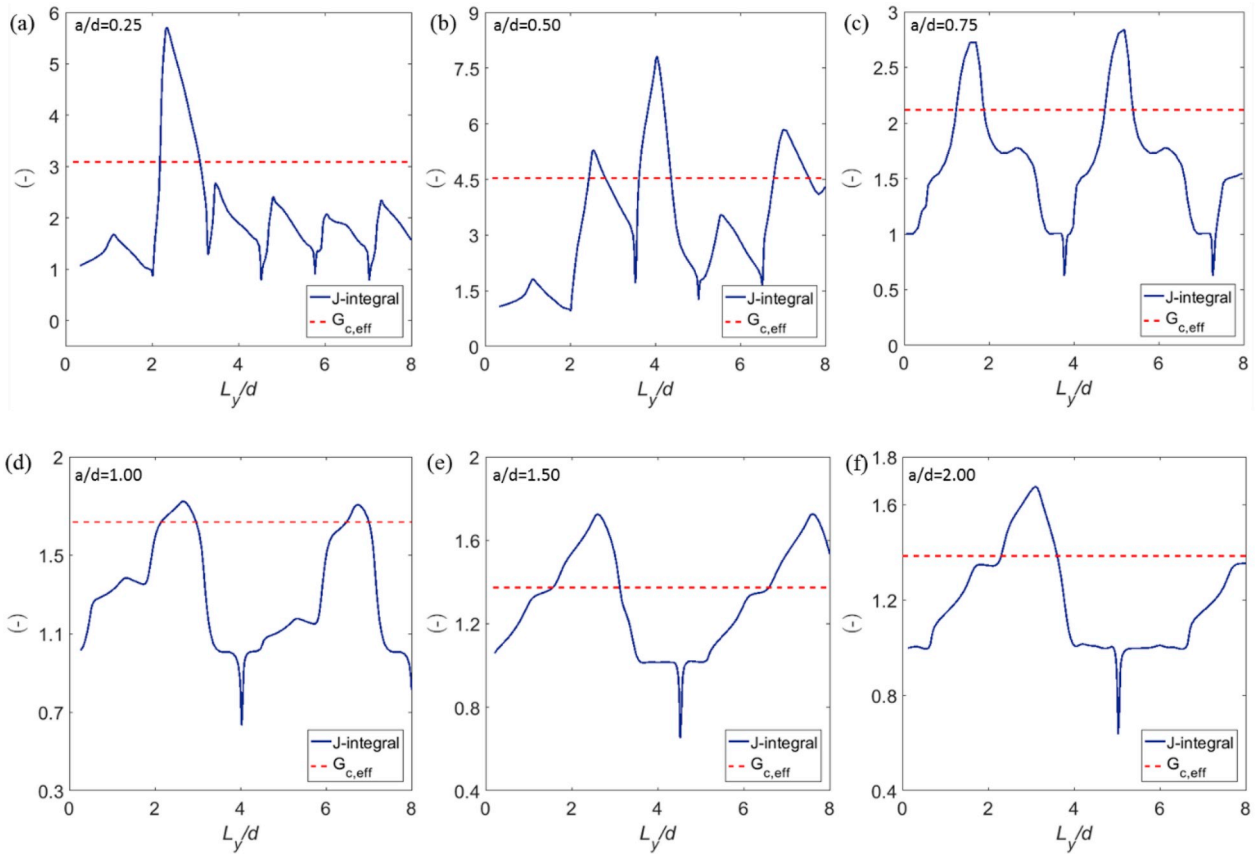

Fig. 17. These plots show normalized J-integral, $\overline{J}$, and effective energy release rate, $G_{c,eff}$, versus relative crack length for series h3. Results for cases with $a/d =$ 0.25, 0.50, 0.75, 1.00, 1.50, and 2.00 are shown in (a–f), respectively.

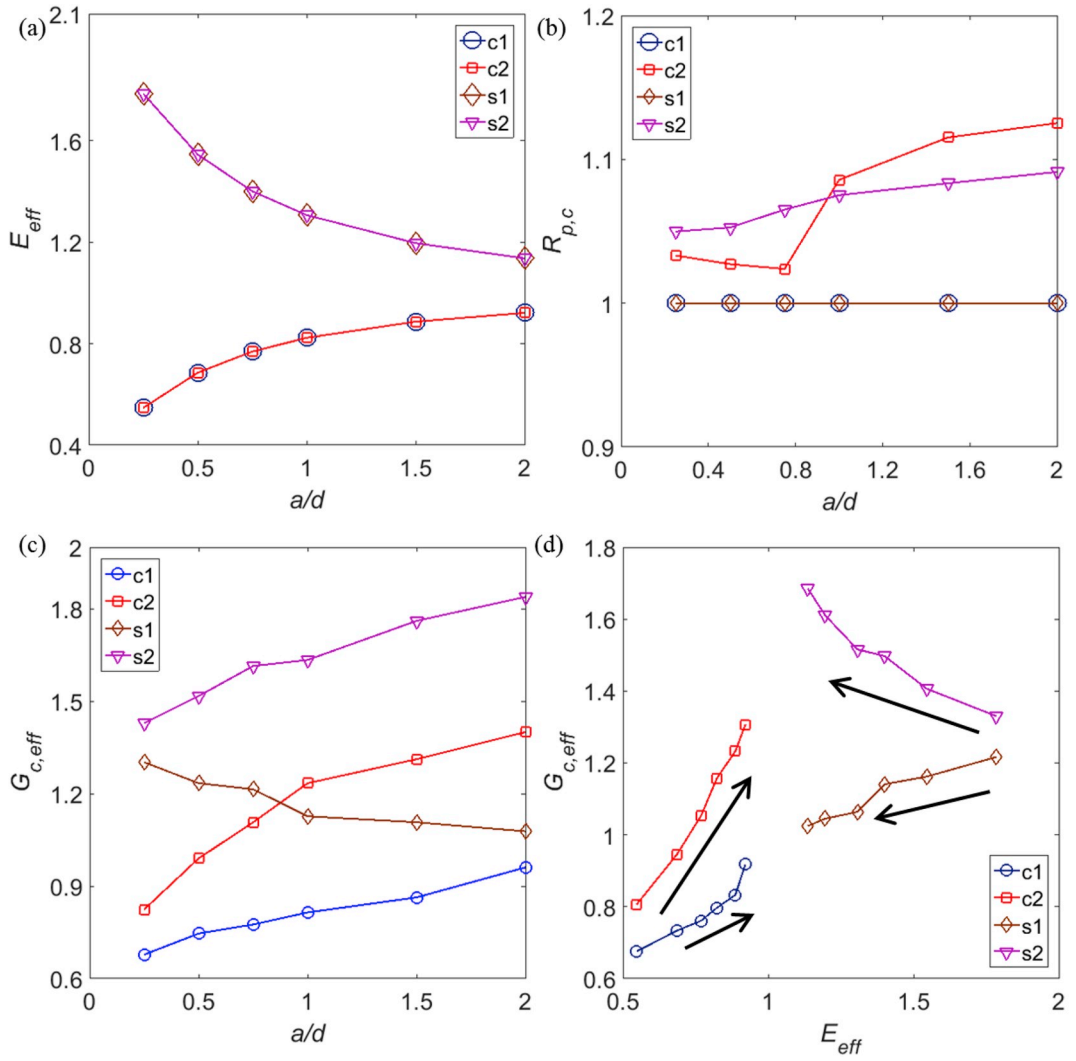

Fig. 18. Fracture variation for series c1, c2, s1, and s2. E_{eff} versus inclusion spacing is shown in (a). $R_{p,c}$, versus inclusion spacing is shown in (b). $G_{c,eff}$ versus inclusion spacing is shown in (c). $G_{c,eff}$ versus E_{eff} is shown in (d), where arrows denote the increasing a/ddirection.

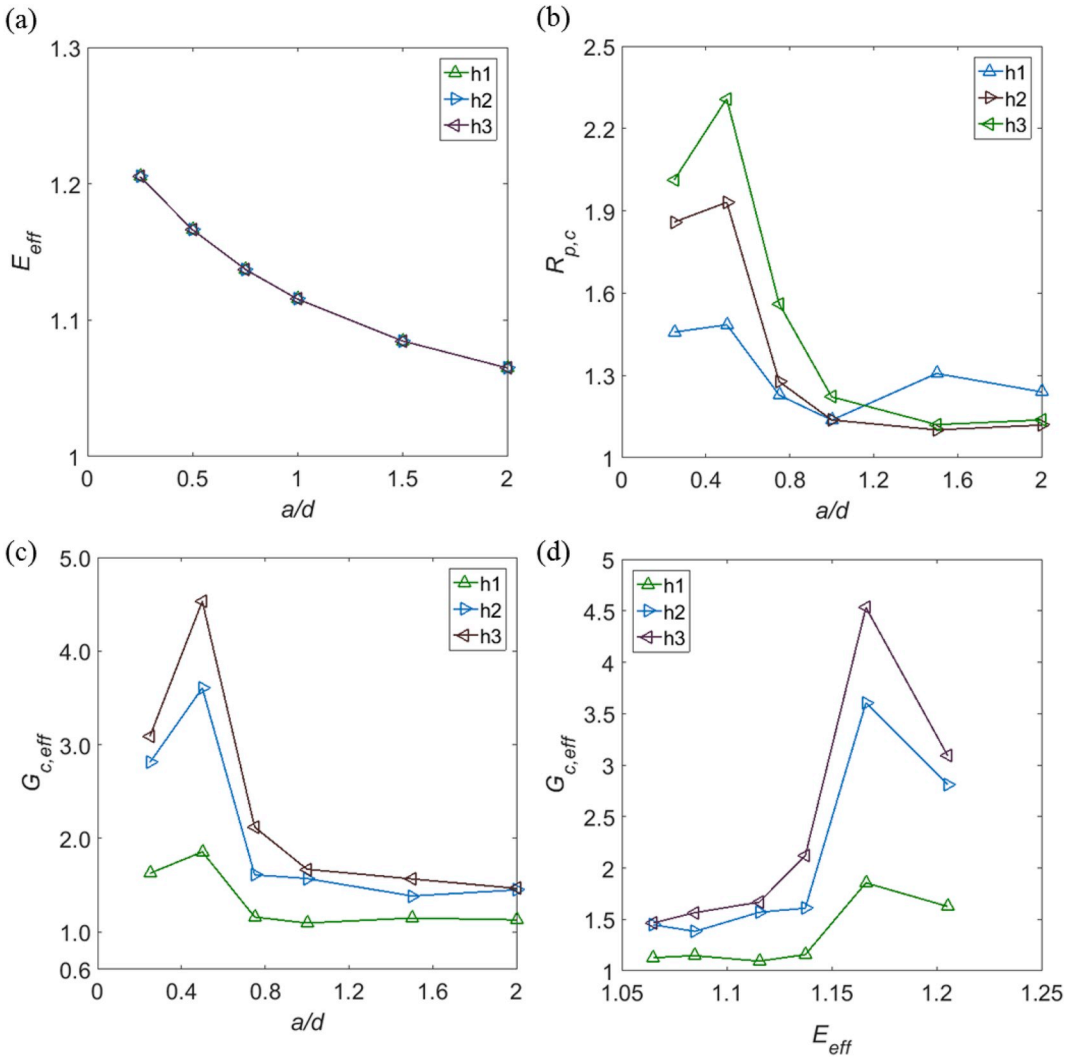

Fig. 19. Fracture variation for series h1, h2, and h3. E_{eff} versus inclusion spacing is shown in (a). $R_{p,c}$, versus inclusion spacing is shown in (b). $G_{c,eff}$ versus inclusion spacing is shown in (c). $G_{c,eff}$ versus E_{eff} is shown in (d).

Appendix

A1. Formulation and Numerical Implementation

The fundamental idea in brittle fracture is that a crack forms in order to minimize the combined strain energy and crack surface energy, which is on the basis of the work by Griffith(1921) [1],

$$U = \int \Omega \backslash \Gamma \psi(\varepsilon) d\Omega + \int_{\Gamma} G_c d\partial\Omega, \tag{A.1}$$

where $\psi(\varepsilon)$ is the strain energy, G_c is the critical energy release rate and the stress is given by $\sigma_{ij} = \partial\psi/\partial\varepsilon_{ij}$. Index notation with the Einstein summation convention is adopted for deviations presented in this work. Comma subscripts are used to denote derivatives with respect to the spatial coordinates. This energy function can be transformed into volume integrals to make it simpler to implement numerically. However, we must replace the normal strain energy density with a damaged strain energy density $\varphi(x) = ((1-\phi)^2 + k)\psi(x,\varepsilon)$, in addition to replacing the surface area energy integral with a regularized volume integral,

$$U = \int_{\Omega} \left[(1-\phi)^2 + k\right] \psi(x,\varepsilon) d\Omega + \int_{\Omega} \frac{G_c}{2} \left(\frac{\phi^2}{\ell_0} + \ell_0 \phi_{,i} \phi_{,i} \right) d\Omega \tag{A.2}$$

where the stress is $\sigma_{ij} = \frac{\partial\varphi}{\partial\varepsilon_{ij}}$. The second term in (A.2) is a continuous representation of the surface energy regarding the phase field damage parameter, ϕ and the crack thickness parameter, ℓ_0. Also, k is a conditioning number for numerical stability. This formulation is adopted from Ref. [28]. Finally, it should be noted that ψ depends on the spatial position x due to the fact that composite materials have spatially-varying elastic moduli due to the different composite phases.

Equilibrium solutions for the displacement, u, and degradation field, ϕ, are assumed to be the ones that minimize the potential energy via the principle of minimum potential energy. The potential energy is the internal energy U minus the work done by external forces V (due to body forces, b, and surface tractions, t). Thus, the external work is

$$V = \int_{\Omega} \rho b_i u_i d\Omega + \int \partial\Omega_t t_i u_i d\partial\Omega_t \tag{A.3}$$

where ρ is the mass density. The portion of the surface where traction (Neumann) boundary conditions are applied is denoted $\partial\Omega_t$. The portion of the surface where displacement boundary conditions, $\bar{u}_i$, are applied is denoted $\partial\Omega_u$, such that the entire surface is the union $\partial\Omega = \partial\Omega_t \cup \partial\Omega_u$Thus, the potential energy is $\Pi = U - W$,

$$\Pi = \int_{\Omega} \varphi(x,\phi,\varepsilon) d\Omega + \int_{\Omega} \frac{G_c}{2} \left(\frac{\phi^2}{\ell_0} + \ell_0 \phi_{,i} \phi_{,i} \right) d\Omega - \int_{\Omega} \rho b_i u_i d\Omega - \int \partial\Omega_t t_i u_i d\partial\Omega \tag{A.4}$$

The equilibrium displacement and damage fields are the minimizers. Taking the first variation with respect to the displacement,

$$D_{\delta u}\Pi = \int_{\Omega} \sigma_{ij} \delta u_{i,j} d\Omega - \int_{\Omega} \rho b_i \delta u_i d\Omega - \int \partial\Omega_t t_i \delta u_i d\partial\Omega \tag{A.5}$$

where the constitutive, $\sigma_{ij} = \frac{\partial\varphi}{\partial\varepsilon_{ij}} = \frac{\partial\varphi}{\partial u_{i,j}}$, was used. Note that we have changed the functional dependence of φ on the strain tensor, ε, to the displacement gradient, ∇u, to simplify the calculations. From the chain rule,

$$\left(\sigma_{ij}\delta u_i\right)_{,j} = \sigma_{ij,j}\delta u_i + \sigma_{ij}\delta u_{i,j} \tag{A.6}$$

as well as the divergence theorem, Eq. (A.5) becomes,

$$D_{\delta u}\Pi = -\int_{\Omega} \left(\sigma_{ij,j} + \rho b_i\right) \delta u_i d\Omega + \int \partial\Omega \left(\sigma_{ij} n_j - t_i\right) \delta u_i d\partial\Omega = 0 \;\forall\; \delta u_i \tag{A.7}$$

Eq. (A.7) should hold for any choice of δu, so it must be the case:

$$\sigma_{ij,j} + \rho b_i = 0 \text{ in } \Omega \tag{A.8a}$$

$$\sigma_{ij} n_j = t_i \text{ on } \partial\Omega, \tag{A.8b}$$

which are the balance of linear momentum equation (or equilibrium equation) and the traction relation.

Computing the derivative of the potential energy with respect to the phase field parameter, φ, and it gives,

$$D_{\delta\phi}\Pi = \int_{\Omega} \left[\frac{\partial\varphi}{\partial\phi}\delta\phi + G_c \left(\frac{\phi\delta\phi}{l_0} + l_0 \phi_{,i} \delta\phi_{,i} \right) \right] d\Omega. \tag{A.9}$$

Using the chain rule for the last term (in index notation) as well as the divergence theorem, Eq. (A.9) could be rewritten as,

$$D_{\delta\phi}\Pi = \int_{\Omega}\left(\frac{\partial\varphi}{\partial\phi}\delta\phi + \frac{G_c\phi\delta\phi}{l_0} - G_c l_0\phi_{,ii}\delta\phi\right)d\Omega + \int \partial\Omega G_c l_0\phi_{,i}n_i\delta\phi d\partial\Omega = 0\ \forall\ \delta\phi \tag{A.10}$$

where $\frac{\partial\varphi}{\partial\phi} = 2(\phi-1)\psi(x,\varepsilon)$ by our definition, $\varphi = [(1-\phi)^2 + k]\psi$. The assumption is made that the fracture energy, G_c, is not spatially varying; this is consistent with the numerical analysis presented in the paper.

Eq. (A.10) should hold for all any choice of $\delta\phi$, it must be the case that:

$$2(\phi-1)\frac{\psi(x,\varepsilon)}{G_c} + \frac{\phi}{l_0} = l_0\phi_{,ii} \text{ in } \Omega, \tag{A.11}$$

$$\phi_{,i}n_i = 0 \text{ on } \partial\Omega. \tag{A.12}$$

We now assume a decomposition of the strain energy density into volumetric, $\psi_{\mathrm{I}}(x,\varepsilon)$, and deviatoric parts, $\psi_{\mathrm{II}}(x,\varepsilon)$, respectively, by replacing $\frac{\psi(x,\varepsilon)}{G_c} = \sqrt{\left(\frac{\psi_{\mathrm{I}}(x,\varepsilon)}{G_{\mathrm{Ic}}}\right)^2 + \left(\frac{\psi_{\mathrm{II}}(x,\varepsilon)}{G_{\mathrm{IIc}}}\right)^2}$, where G_{Ic} and G_{IIc} are the corresponding critical energy release rates in mode I and II. Substituting the strain energy decomposition into Eq. (A.11) gives

$$2(\phi-1)\sqrt{\left(\frac{\psi_{\mathrm{I}}(x,\varepsilon)}{G_{\mathrm{Ic}}}\right)^2 + \left(\frac{\psi_{\mathrm{II}}(x,\varepsilon)}{G_{\mathrm{IIc}}}\right)^2} + \frac{\phi}{l_0} = l_0\phi_{,ii} \tag{A.13}$$

The governing partial differential equations are summarized as follows:

$$\sigma_{ij,j} + b_i = 0 \text{ in } \Omega \tag{A.14a}$$

$$\sigma_{ij}n_j = t_i \quad \text{on } \partial\Omega_t \tag{A.14b}$$

$$u_i = \overline{u}_i \text{ on } \partial\Omega_u, \tag{A.14c}$$

$$2(\phi-1)\sqrt{\left(\frac{\psi_{\mathrm{I}}(x,\varepsilon)}{G_{\mathrm{Ic}}}\right)^2 + \left(\frac{\psi_{\mathrm{II}}(x,\varepsilon)}{G_{\mathrm{IIc}}}\right)^2} + \frac{\phi}{l_0} = l_0\phi_{,ii} \text{ in } \Omega, \tag{A.14d}$$

$$\phi_{,i}n_i = 0 \text{ on } \partial\Omega. \tag{A.14e}$$

A2. Model Validation

A.2.1 Validation with elastic fracture mechanics

As shown in Fig. A1, a scenario of a classical crack problem was simulated to validate the model and implementation. An elliptical crack with the long axis (along *x*-direction) being 1 mm and the short axis (along *y*-direction) being 0.01 mm was located in the center of the square domain shown in Fig. A1(d). This domain was fixed on the lower boundary along the *x*- and *y*-directions and displacements were applied on the upper boundary in both the *x*- and *y*-directions, forming a mixed-mode loading on the pre-crack.

In the two-dimensional plane strain setting, 3-node triangle elements with element sizes no greater than 1/10 of the pre-crack length were used. The element size around the pre-crack tip was 0.01 mm.

The values of the various material properties were as follows: Young's modulus was 2×10^5 MPa, Poisson's ratio was 0.25, the critical energy release rate was set to a sufficiently large value (9.9×10^4 N/mm) to ensure that the crack would not propagate. In this way, the analytical results from linear elastic fracture mechanics can be compared to the numerical solution. As for the boundary conditions, the displacement on the bottom surface was set to zero in both the *x*- and *y*-directions, while top surface was loaded by applying displacements $u_y = 0.05$ mm and $u_x = 0.025$ mm, in the *x*- and *y*-directions, respectively.

According to classic linear elastic fracture mechanics, the displacement fields around the crack tip for mode-I are

$$u_x^I = \frac{K_I}{2\mu}\sqrt{\frac{r}{2\pi}}\cos\left(\frac{\theta}{2}\right)\left[\kappa - 1 + 2\sin^2\left(\frac{\theta}{2}\right)\right] \tag{A.15a}$$

$$u_y^I = \frac{K_I}{2\mu}\sqrt{\frac{r}{2\pi}}\sin\left(\frac{\theta}{2}\right)\left[\kappa + 1 - 2\cos^2\left(\frac{\theta}{2}\right)\right] \tag{A.15b}$$

where, $K_I = \sigma\sqrt{a\pi}$ is the mode-I fracture toughness, with a being half of the crack length (long axis) and σ being the far field tensile stress. $K_{II} = \tau\sqrt{a\pi}$ is the mode-2 fracture toughness, with τ being the far field shear stress. The polar coordinates r and θ were used with the crack tip being the origin along $= 0$. Also, the displacement fields around the crack tip for mode-II are

$$u_x^{II} = \frac{K_{II}}{2\mu}\sqrt{\frac{r}{2\pi}}\sin\left(\frac{\theta}{2}\right)\left[\kappa + 1 + 2\cos^2\left(\frac{\theta}{2}\right)\right] \tag{A.16a}$$

$$u_y^{II} = \frac{K_{II}}{2\mu}\sqrt{\frac{r}{2\pi}}\cos\left(\frac{\theta}{2}\right)\left[\kappa - 1 - 2\sin^2\left(\frac{\theta}{2}\right)\right] \tag{A.16b}$$

The total displacement field is then

$$u_x = u_x^I + u_x^{II} \tag{A.17a}$$

$$u_y = u_y^I + u_y^{II} \tag{A.17b}$$

The x- and y-displacement data from the result file of ABAQUS along the line of $x = 0.5$ mm around the crack tip area was extracted and compared with analytical results. Fig. A1 (b-c) shows that the modeling results are in good agreement with the analytical results.

A.2.2 Validation of mixed-mode fracture with inclusions

A series of cases were studied to verify the phase-field model both for mode-I and mode-II fracture. To validate mode-I fracture, a plate with area (width and height) $\times h = 3$ mm $\times$ 4 mm , as shown in Fig. A2(a), was used. A horizontal pre-crack was arranged at the middle of left edge with a length of 1 mm. A compliant or stiff inclusion was located in the center of the plate with a pre-crack pointing towards it along the horizontal axis (also an axis of symmetry). The radius of the inclusion was fixed as $r = 0.3$ mm for all cases. The distance between the pre-crack tip and edge of the inclusion, shown as d in Fig. A. 2(a), was varied between the values $0.5r$, $1.0r$, and $1.5r$. The problem used to validate mode-II fracture was identical to that used for mode-I fracture but with a different displacement control of the top surface, to create a mode-II fracture scenario.

According to the work of Zhonghua Li et al. [42], the change in the stress intensity factor (SIF) of a mode-I crack tip in presence of an inclusion is

$$\frac{\Delta K_{I,tip}}{K_{I,0}} = \frac{1}{\pi}\int_A r^{-2}\left(C_1 \cos\frac{\theta}{2}\cos\frac{3\theta}{2} + C_2 \sin^2\theta\cos\theta\right)dA, \tag{A.18}$$

where $K_{I,0}$ is the mode-I SIF for the crack tip without inclusions, $\Delta K_{I,\,tip} = K_{I,tip} - K_{I,0}$ is the change in SIF. The variable, A, is the upper half of the area of the inclusion. The polar coordinates are r and θ with the crack tip being the origin along $\theta = 0$. The parameters C_1 and C_2 are related to the material properties and are given by

$$C_1 = \frac{(1-\alpha)(1-2\nu)}{(1+\alpha-2\nu)} \tag{A.19a}$$

$$C_2 = \frac{3(1-\alpha)}{2(1+3\alpha-4\nu\alpha)} \tag{A.19b}$$

where α is the ratio of the Young's modulus of the inclusion to the Young's modulus of the matrix. The Poisson ratio (assumed equal for the inclusion and matrix) is given by ν.

As for the mode-II problem, the change in the SIF is [43],

$$\frac{\Delta K_{II,tip}}{K_{II,0}} = \frac{1}{\pi}\int_A r^{-2}(D_1\cos\theta + D_2\cos 2\theta + D_3\cos 3\theta)dA, \tag{A.20}$$

where D_1, D_2, and D_3 are parameters related to the material properties:

$$D_1 = \frac{(1-\alpha)(11+19\alpha+32\nu^2\alpha-22\nu-40\nu\alpha)}{16(1+\alpha-2\nu)(1+3\alpha-4\nu\alpha)} \tag{A.21a}$$

$$D_2 = -\frac{(1-\alpha)(1-2\nu)}{16(1+\alpha-2\nu)} \tag{A.21b}$$

$$D_3 = \frac{9(1-\alpha)}{16(1+3\alpha-4\nu\alpha)} \tag{A.21c}$$

The other parameters follow the previous definitions.

The change in the energy release rate is then given by

$$\frac{\Delta G_{tip}}{G_0} = \frac{G_{tip}}{G_0} - 1 = \frac{\left(K_0 + \Delta K_{tip}\right)^2}{K_0^2} - 1 = 2\frac{\Delta K_{tip}}{K_0} + \left(\frac{\Delta K_{tip}}{K_0}\right)^2 \tag{A.22}$$

Eq. (A.22) holds for mode-I and mode-II fracture.

To conduct the analysis with a normalized mechanical property system rather than specific values, for each case with compliant or stiff inclusions, a conjugate case with identical geometry and no inclusions was also modeled as a comparison. The critical energy release rate was set with a large value of 999.0 N/mm to ensure no crack propagation occurs. The J-integral was extracted and compared to study the influence of the compliant and stiff inclusions.

The comparison between the analytical solution and the model is shown in Fig. A. 2(b-c) for mode-I fracture and Fig. A. 3(b-c) for mode-II fracture. The normal and shear stress distributions are shown in Fig. A. 2(d-i) for mode-I fracture and Fig. A. 3(d-i) for mode-II fracture, respectively. It should be noted that to keep this part concise, only the stress distribution for the case with $\frac{d}{r} = 0.5$ is included. The change of energy release rate obtained from modeling fits well with the analytical solutions.

A.2.3 Validation of kinked fracture

Considering the effect of compliant and stiff inclusions on the crack propagation, the accuracy of the phase-field model for simulating kinked fracture was also verified.

A plate with width and height of $b \times h = 3$ mm $\times$ 4 mm (see Fig. A4) with a horizontal pre-crack arranged at the middle of left edge of length of

$l = 1$ mm is used. A kink was then added to the original crack tip with a length of $0.1l$. The angle between the pre-crack and kink, denoted as θ, is varied from -60° to 60°. For all cases in this section, the displacement at bottom surface was zero (in both directions) and the top surface was stretched uniformly along vertical direction. The mode-I and mode-II SIFs around the kink tip are then extracted with the interaction integral method [44].

Based on work of Wu [45], the SIFs at the kinked crack tip can be expressed as:

$$k_I = [K_I a_{11}(\theta) + K_{II} b_{11}(\theta)] + T\sqrt{\frac{8l}{\pi}}\sin^2\theta + \sqrt{\frac{2}{\pi}}l[C_3 a_{13}(\theta) + D_3 b_{13}(\theta)] \tag{A.23a}$$

$$k_{II} = [K_I a_{21}(\theta) + K_{II} b_{21}(\theta)] - T\sqrt{\frac{8l}{\pi}}\sin\theta\cos\theta + \sqrt{\frac{2}{\pi}}l[C_3 a_{23}(\theta) + D_3 b_{23}(\theta)] \tag{A.23b}$$

where, K_I, K_{II}, and T are the mode-I, mode-II, and T-stress for the original crack tip, respectively. The length of the kink is l. The parameters a_{mn} and b_{mn} are related to θ by

$$a_{11}(\theta) = \frac{1}{4}\cos\left(\frac{3}{2}\theta\right) + \frac{3}{4}\cos\left(\frac{1}{2}\theta\right) \tag{A.24a}$$

$$b_{11}(\theta) = -\frac{3}{4}\sin\left(\frac{3}{2}\theta\right) - \frac{3}{4}\sin\left(\frac{1}{2}\theta\right) \tag{A.24b}$$

$$a_{13}(\theta) = -\frac{3}{4}\cos\left(\frac{5}{2}\theta\right) + \frac{15}{4}\cos\left(\frac{1}{2}\theta\right) \tag{A.24c}$$

$$b_{13}(\theta) = -\frac{15}{4}\sin\left(\frac{5}{2}\theta\right) + \frac{15}{4}\sin\left(\frac{1}{2}\theta\right) \tag{A.24d}$$

$$a_{21}(\theta) = \frac{1}{4}\sin\left(\frac{3}{2}\theta\right) + \frac{1}{4}\sin\left(\frac{1}{2}\theta\right) \tag{A.24e}$$

$$b_{21}(\theta) = \frac{3}{4}\cos\left(\frac{3}{2}\theta\right) + \frac{1}{4}\cos\left(\frac{1}{2}\theta\right) \tag{A.24f}$$

$$a_{23}(\theta) = -\frac{3}{4}\sin\left(\frac{5}{2}\theta\right) + \frac{3}{4}\sin\left(\frac{1}{2}\theta\right) \tag{A.24g}$$

$$b_{23}(\theta) = \frac{15}{4}\cos\left(\frac{5}{2}\theta\right) - \frac{3}{4}\cos\left(\frac{1}{2}\theta\right) \tag{A.24h}$$

The parameters C_3 and D_3 are the third order coefficients of the Williams series expansion.

The comparison between the phase field model and analytical results is shown in Fig. 4(b) with the x-axis showing the ratio of the mode-I and mode-II SIF around the kink tip. For brevity, only the stress distribution for $\theta = 40^\circ$ is presented in Fig. 4(c–e).The modeling results fit well with the analytical solutions.

A.2.4 Comparison of different fracture criteria

To understand the difference between the phase field methods adopting different fracture criteria, a series of cases were modeled. The two fracture criteria adopted in this part are: (1) the linear mixed mode criterion defined as $\frac{\psi_I(\varepsilon)}{G_{Ic}} + \frac{\psi_{II}(\varepsilon)}{G_{IIc}}$ and (2), the quadratic mixed mode criterion defined as $\sqrt{\left(\frac{\psi_I(x,\varepsilon)}{G_{Ic}}\right)^2 + \left(\frac{\psi_{II}(x,\varepsilon)}{G_{IIc}}\right)^2}$. Two UEL subroutines in ABAQUS were implemented and utilized in these two cases with identical geometry.

As shown in Fig. A. 5(a), a plate with a width and height of $b \times h = 3$ mm $\times$ 4 mm was used. A horizontal pre-crack was arranged at the middle of the left edge with a length of 1 mm. No inclusions were included in this modeling. Mixed-mode fracture cases were modeled for each series, where the top surface was displaced in the horizontal and vertical directions by 0.1 mm. The phase field distributions for each case are shown in Fig. A. 5(b-c). It can be observed that with the quadratic criterion, the damaged part of the phase field becomes more localized around the crack, which demonstrates that the quadratic criterion captures sharp cracks in brittle materials more accurately than a linear criterion.

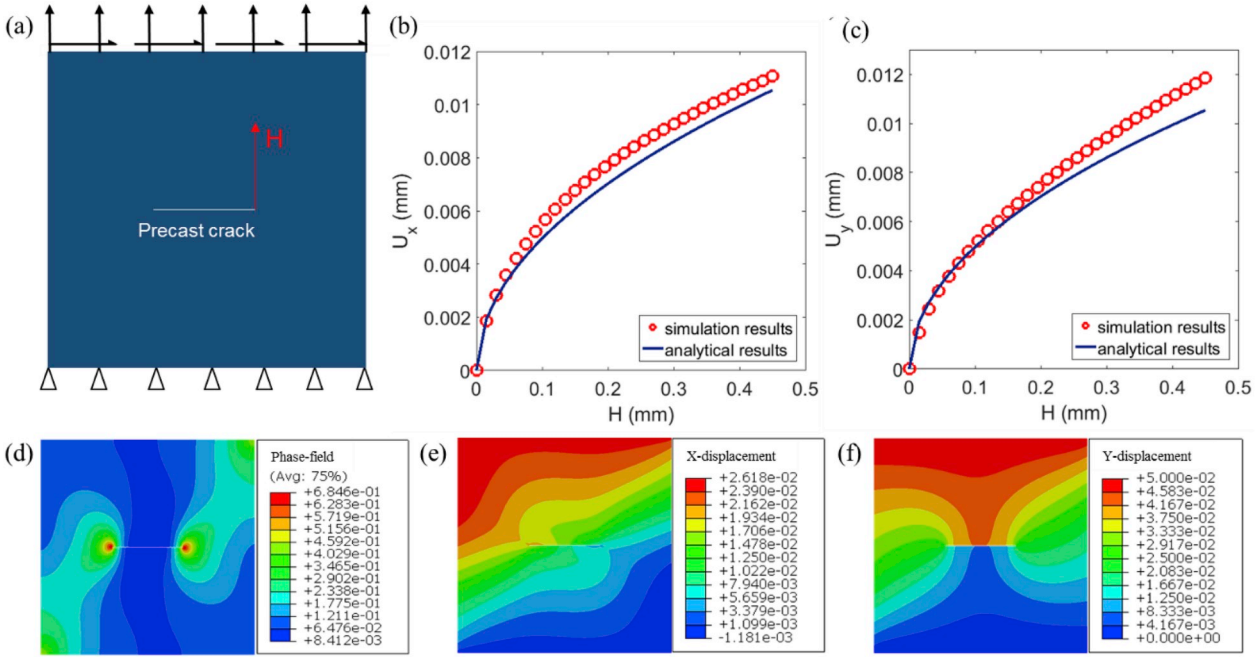

Fig. A.1. Phase-field model validation. The geometry and loading conditions are shown in (a). The model prediction and analytical results of the *x*-component of displacement is shown in (b) and of the *y*-component of displacement in (c) along the line $x = 0.05$ mm. The contour plot of the phase field damage parameter is shown in (d). Contour plots of the displacement field in the *x*- and *y*-directions are shown in (e) and (f), respectively.

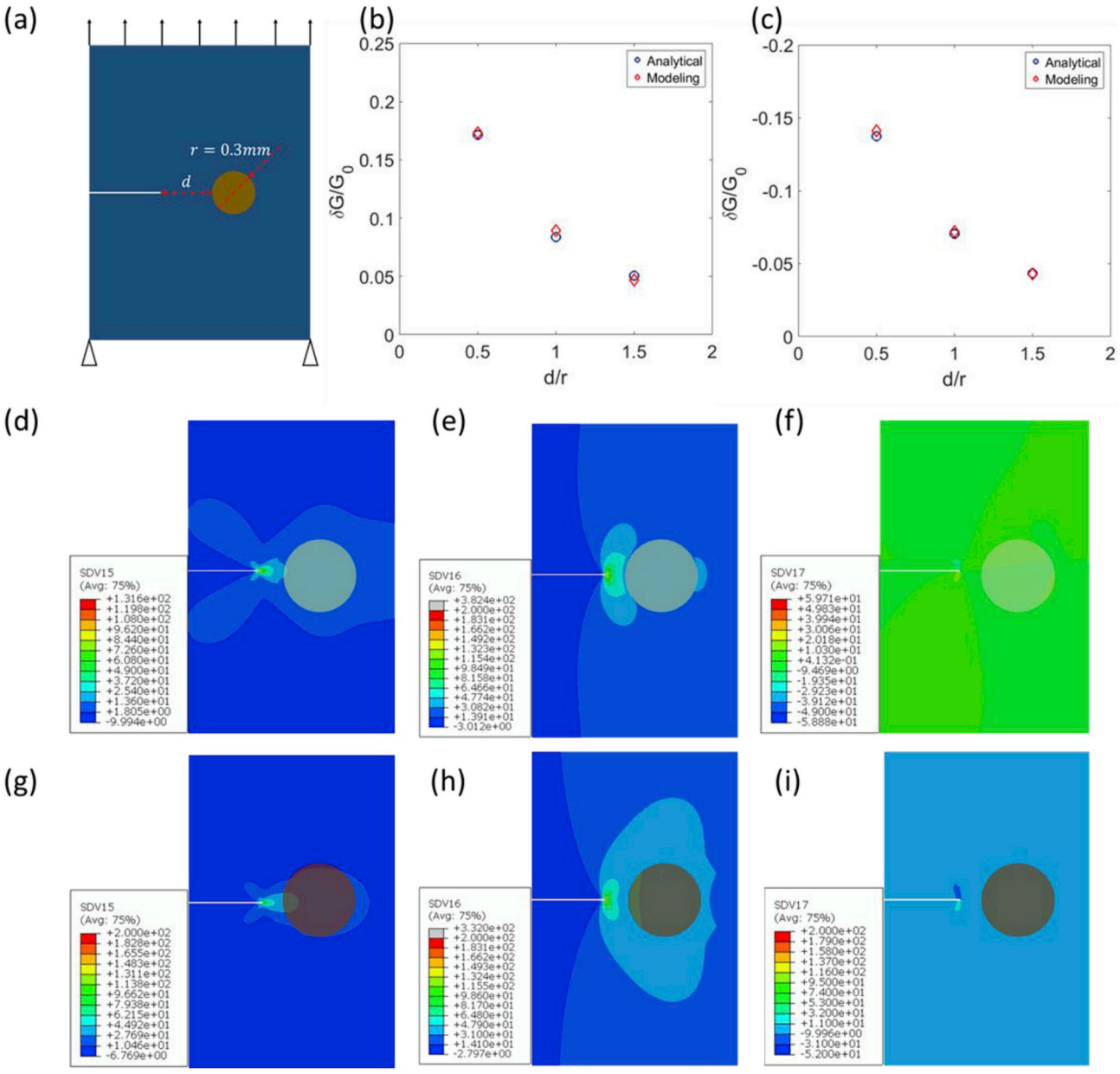

Fig. A.2. Validation of mode-I fracture with inclusions. The problem geometry is shown in (a). The comparison between the analytical solution and phase field model for compliant and stiff inclusions are shown in (b) and (c), respectively. The stress components σ_{11}, σ_{22} and σ_{12} of the case with compliant inclusions are shown in (d-f) and the case with stiff inclusions are shown in (g-i) (both cases assume $d/r = 0.5$).

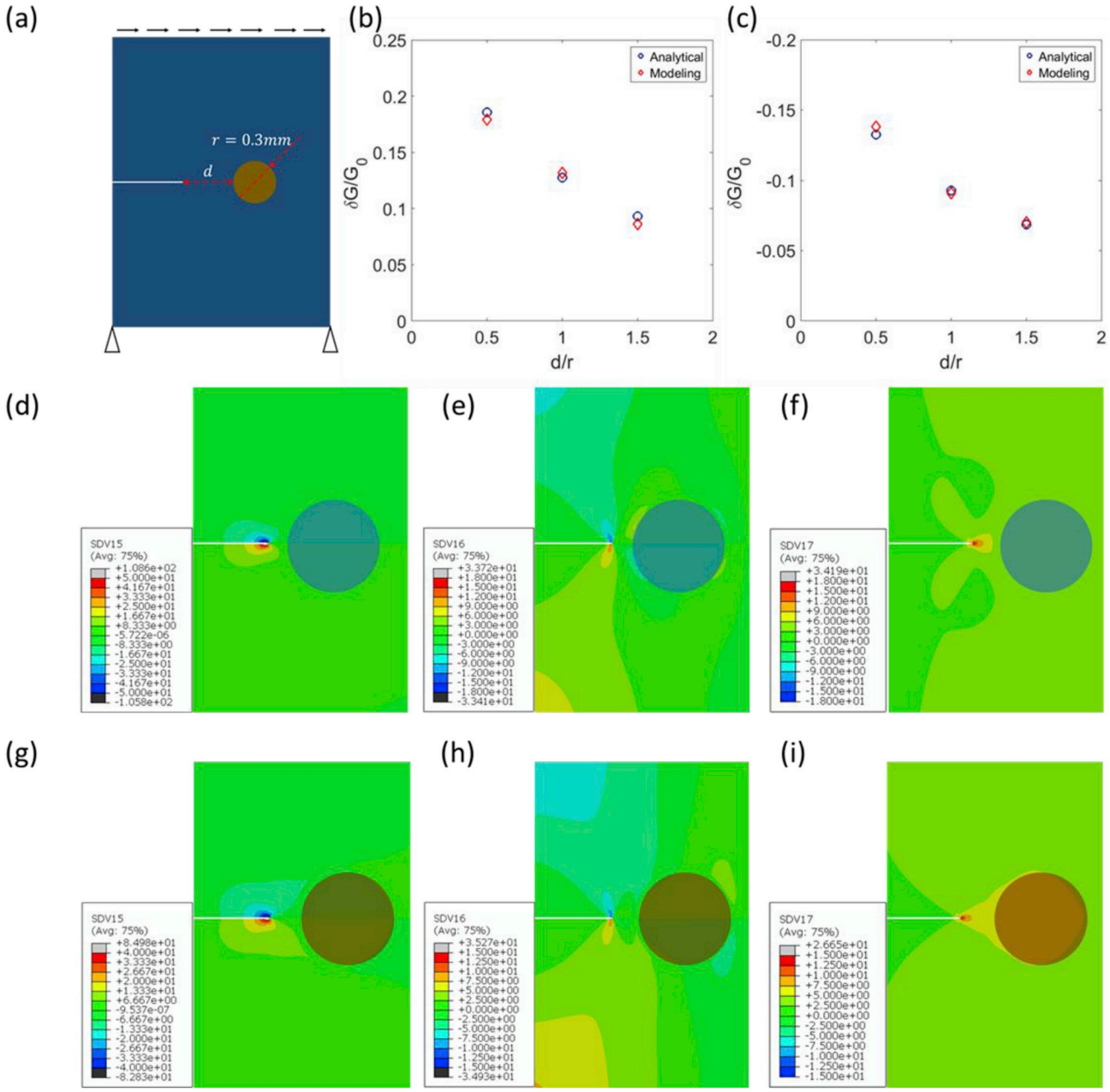

Fig. A.3. Validation of mode-II fracture with inclusions. The geometry is shown in (a). The comparison between the analytical solution and phase field model for compliant and stiff inclusions is shown in (b) and (c), respectively. The stress components σ_{11}, σ_{22}, and σ_{12} of the case with compliant inclusions are shown in (d-f) and the case with stiff inclusions are shown in (g-i) (both cases assume d/r = 0.5).

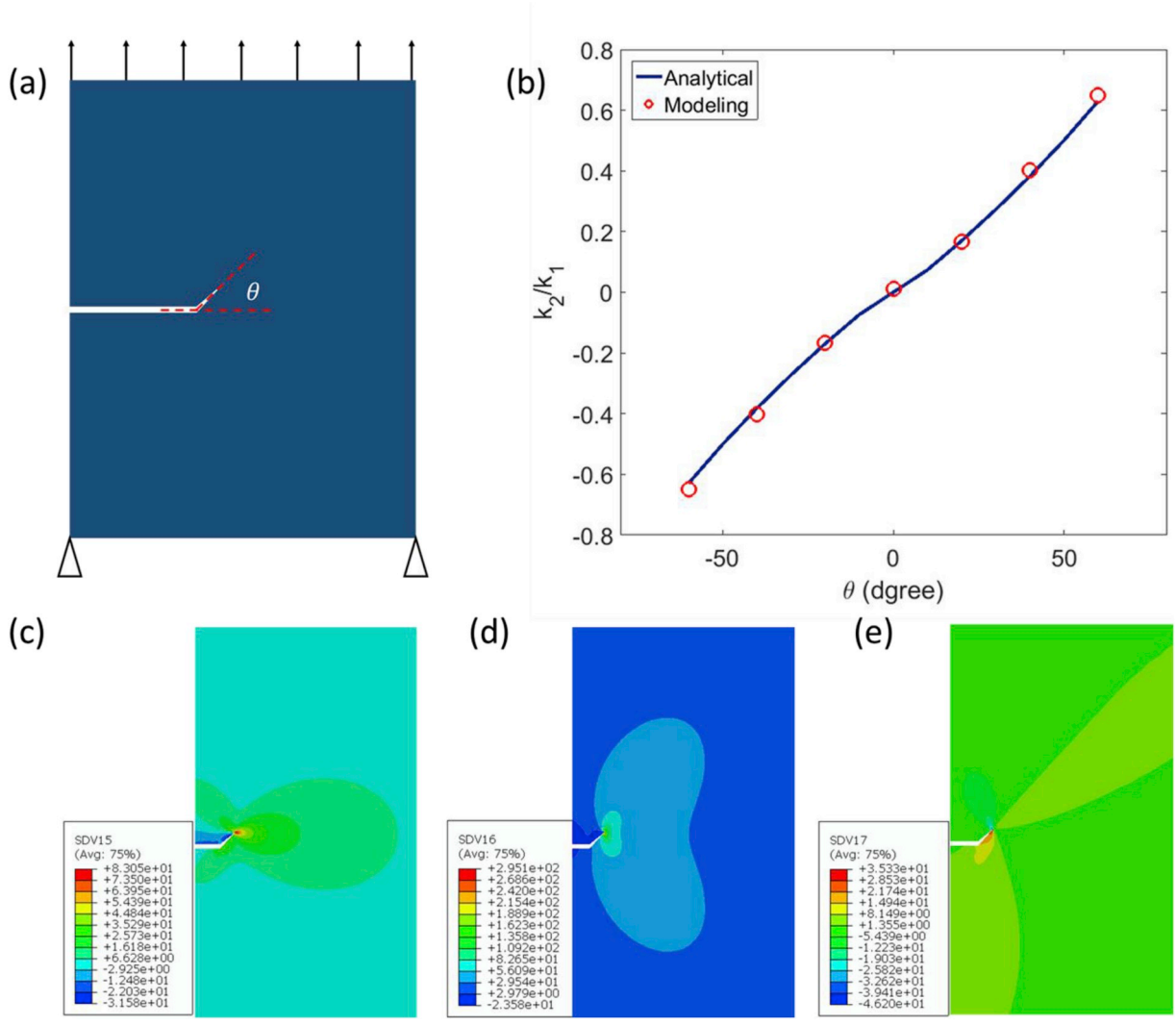

Fig. A.4. Validation of kinked fracture. The geometry is shown in (a). The comparison between the analytical solution and the phase field model is shown in (b). The stress components σ_{11}, σ_{22}, and σ_{12} (evaluated at $\theta = 40°$) are shown in (c-e).

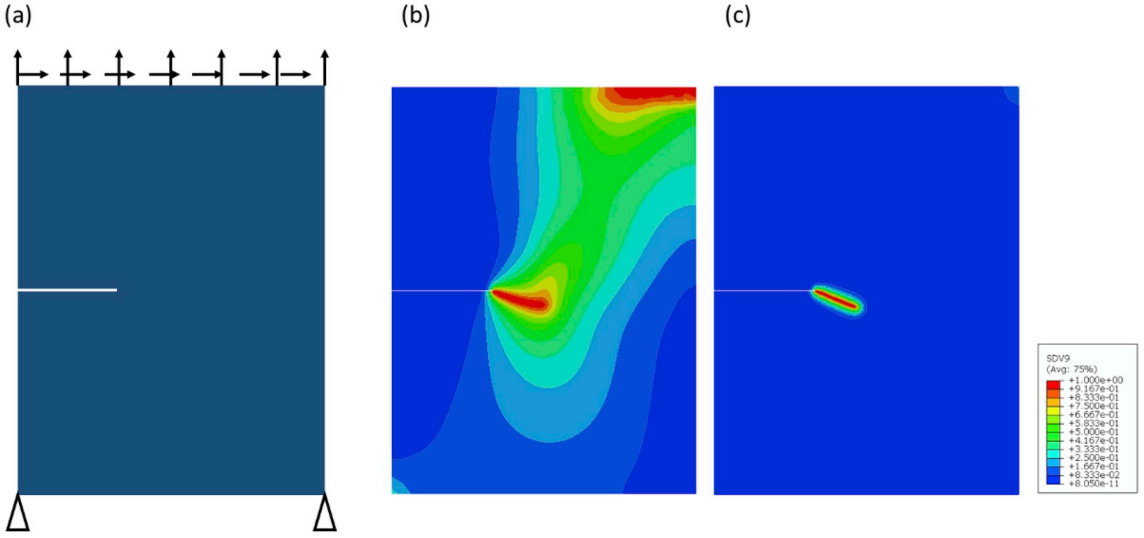

Fig. A.5. Comparison between phase field models adopting different fracture criteria. The geometry is shown in (a). The distribution of the fracture parameter, ϕ, for the case with a linear fracture criterion is shown in (b) and (c) shows the distribution for the case with a quadratic fracture criterion.

References

[1] Griffith AA, Eng M. VI. The phenomena of rupture and flow in solids. Phil Trans Roy Soc Lond 1921;221(582–593):163–98.
[2] Bower AF, Ortiz M. A three-dimensional analysis of crack trapping and bridging by tough particles. J Mech Phys Solids 1991;39(6):815–58.
[3] Bower A, Ortiz M. The influence of grain size on the toughness of monolithic ceramics. J Eng Mater Technol 1993;115(3):228–36.
[4] Faber KT, Evans AG. Crack deflection processes—I. *Theor.* Acta metall 1983;31(4):565–76.
[5] Suresh S, Shih C, Morrone A, O'Dowd N. Mixed-mode fracture toughness of ceramic materials. J Am Ceram Soc 1990;73(5):1257–67.
[6] Huajian G. Fracture analysis of nonhomogeneous materials via a moduli-perturbation approach. Int J Solids Struct 1991;27(13):1663–82.
[7] Hossain MZ, Hsueh CJ, Bourdin B, Bhattacharya K. Effective toughness of heterogeneous media. J Mech Phys Solids 2014;71:15–32.
[8] Cai H, Faber K. On the use of approximation methods for microcrack shielding problems. J Appl Mech 1992;59(3):497–501.
[9] Muju S. Crack propogation in bimaterial multilayered periodically microcracking composite media. Compos Sci Technol 2000;60(12–13):2213–21.
[10] Xuyue W, Duo W, Zhenzhu Z. On the Griffith crack in a nonhomogeneous interlayer of adjoining two different elastic materials. Int J Fract 1996;79(3):R51–6.
[11] Yu H, Wu L, Guo L, Du S, He Q. Investigation of mixed-mode stress intensity factors for nonhomogeneous materials using an interaction integral method. Int J Solids Struct 2009;46(20):3710–24.
[12] Hoteit H, Firoozabadi A. Multicomponent fluid flow by discontinuous Galerkin and mixed methods in unfractured and fractured media. Water Resour Res 2005;41(11).
[13] Blackman BRK, Hadavinia H, Kinloch AJ, Williams JG. The use of a cohesive zone model to study the fracture of fibre composites and adhesively-bonded joints. Int J Fract 2003;119(1):25–46.
[14] Bažant Zdeněk P, Lin FB. Nonlocal smeared cracking model for concrete fracture. J Struct Eng 1988;114(11):2493–510.
[15] Lotfi H, Shing P. An appraisal of smeared crack models for masonry shear wall analysis. Comput Struct 1991;41(3):413–25.
[16] Borden MJ, Verhoosel CV, Scott MA, Hughes TJR, Landis CM. A phase-field description of dynamic brittle fracture. Comput Methods Appl Mech Eng 2012;217–220:77–95.
[17] Li J-b, Gao X, Fu X-a, Wu C, Lin G. A nonlinear crack model for concrete structure based on an extended scaled boundary finite element method. Appl Sci 2018;8(7):1067.
[18] Li J-b, Fu X-a, Chen B-b, Wu C, Lin G. Modeling crack propagation with the extended scaled boundary finite element method based on the level set method. Comput Struct 2016;167:50–68.
[19] Rashid YR. Ultimate strength analysis of prestressed concrete pressure vessels. Nucl Eng Des 1968;7(4):334–44.
[20] Francfort GA, Marigo JJ. Revisiting brittle fracture as an energy minimization problem. J Mech Phys Solids 1998;46(8):1319–42.
[21] Bourdin B, Francfort GA, Marigo J-J. The variational approach to fracture, vol. 91; 2008 (1-3): pp. 5–148.
[22] Tanné E, Li T, Bourdin B, Marigo JJ, Maurini C. Crack nucleation in variational phase-field models of brittle fracture. J Mech Phys Solids 2018;110:80–99.
[23] Badnava H, Msekh MA, Etemadi E, Rabczuk T. An h-adaptive thermo-mechanical phase field model for fracture. Finite Elem Anal Des 2018;138:31–47.
[24] Dedè L, Borden MJ, Hughes TJ. Isogeometric analysis for topology optimization with a phase field model. Arch Comput Methods Eng 2012;19(3):427–65.
[25] Wu T, Carpiuc-Prisacari A, Poncelet M, De Lorenzis L. Phase-field simulation of interactive mixed-mode fracture tests on cement mortar with full-field displacement boundary conditions. Eng Fract Mech 2017;182:658–88.
[26] Bryant EC, Sun W. A mixed-mode phase field fracture model in anisotropic rocks with consistent kinematics. Comput Methods Appl Mech Eng 2018;342:561–84.
[27] Huynh GD, Zhuang X, Nguyen-Xuan H. Implementation aspects of a phase-field approach for brittle fracture. Front Struct Civ Eng 2018.
[28] Msekh MA, Sargado JM, Jamshidian M, Areias PM, Rabczuk T. Abaqus implementation of phase-field model for brittle fracture. Comput Mater Sci 2015;96:472–84.
[29] Kuhn C, Schlüter A, Müller R. On degradation functions in phase field fracture models. Comput Mater Sci 2015;108:374–84.
[30] Zhang X, Sloan SW, Vignes C, Sheng D. A modification of the phase-field model for mixed mode crack propagation in rock-like materials. Comput Methods Appl Mech Eng 2017;322:123–36.
[31] Shetty D, Rosenfield A, Duckworth W. Mixed-mode fracture of ceramics in diametral compression. J Am Ceram Soc 1986;69(6):437–43.
[32] Bradt RC. Fracture mechanics of ceramics, vol. 8; 1986.
[33] Li M, Sakai M. Mixed-mode fracture of ceramics in asymmetric four-point bending: effect of crack-face grain interlocking/bridging. J Am Ceram Soc 1996;79(10):2718–26.
[34] Fett T, Gerteisen G, Hahnenberger S, Martin G, Munz D. Fracture tests for ceramics under mode-I, mode-II and mixed-mode loading. J Eur Ceram Soc 1995;15(4):307–12.
[35] Singh D, Shetty DK. Fracture toughness of polycrystalline ceramics in combined mode I and mode II loading. J Am Ceram Soc 1989;72(1):78–84.
[36] Belli R, Wendler M, Petschelt A, Lohbauer U. Mixed-mode fracture toughness of texturized LS2 glass-ceramics using the three-point bending with eccentric notch test. Dent Mater 2017;33(12):1473–7.
[37] Thakur AR, Wei C, Wu C, Wojnar CS. Determining the E_ective strength and fracture toughness of ceramic composites with ordered inclusions. Under review. 2019.
[38] Aluminum Oxide, Al2O3 Ceramic Properties. [cited 2019; Available from: https://accuratus.com/alumox.html.
[39] Alumina - Aluminium Oxide - Al2O3 - A Refractory Ceramic Oxide. [cited 2019; Available from: https://www.azom.com/properties.aspx?ArticleID=52.
[40] Zhao J, Stearns LC, Harmer MP, Chan HM, Miller GA, Cook RF. Mechanical behavior of alumina–silicon carbide „nanocomposites". J Am Ceram Soc 1993;76(2):503–10.
[41] Baskaran S, Halloran JW. Fibrous monolithic ceramics: II, flexural strength and fracture behavior of the silicon carbide/graphite system. J Am Ceram Soc 1993;76(9):2217–24.
[42] Li Z, Chen Q. Crack-inclusion interaction for mode I crack analyzed by Eshelby equivalent inclusion method. Int J Fract 2002;118(1):29–40.
[43] Yang L, Chen Q, Li Z. Crack–inclusion interaction for mode II crack analyzed by Eshelby equivalent inclusion method. Eng Fract Mech 2004;71(9–10):1421–33.
[44] Daimon R, Okada H. Mixed-mode stress intensity factor evaluation by interaction integral method for quadratic tetrahedral finite element with correction terms. Eng Fract Mech 2014;115:22–42.
[45] Li Y, Sun T, Gao Q, Tan C. A stress intensity factor estimation method for kinked crack. Eng Fract Mech 2018;188:202–16.